Numerical study of the wake characteristics of a notchback Ahmed body

Newton Fabrice Ouedraogo

A Thesis

in

The Department

of

Mechanical Industrial and Aerospace Engineering

Presented in Partial Fulfillment of the Requirements

for the Degree of

Master of Applied Science (Mechanical Engineering) at

Concordia University

Montreal, Quebec, Canada

December 2023

Concordia University

School of Graduate Studies

This is to certify that the thesis prepared

By: Newton Fabrice Ouedraogo

Entitled: Numerical study of the wake characteristics of a notchback Ahmed body

and submitted in partial fulfillment of the requirements for the degree of

Master of Applied Science (Mechanical Engineering)

complies with the regulations of this University and meets the accepted standards with respect to originality and quality.

Signed by the final Examining Committee:

_____ Chair

Dr. Lyes Kadem

_____ Examiner

Dr. Lyes Kadem

_____ Examiner

Dr. Hoi Dick Ng

_____ Supervisor

Dr. Ebenezer Ekow Essel

Approved by _____

Martin D. Pugh, Chair

Department of Mechanical, Industrial and Aerospace Engineering

_____ 2023 _____

Mourad Debbabi, Dean

Gina Cody School of Engineering and Computer Science

Abstract

Numerical study of the wake characteristics of a notchback Ahmed body

Newton Fabrice Ouedraogo

This thesis investigates the effects of Reynolds number on the wake characteristics of a notchback Ahmed body with effective backlight angle, $\beta_e = 17.8°$. The Reynolds number based on the body height was varied from 5×10^3 to 5×10^4. Prior to the Reynolds number investigation, a Reynolds-Averaged Navier-Stokes (RANS) model assessment was performed using nine turbulence models consisting of one- and two-equation eddy-viscosity models and second moment closure models. The standard Spalart-Allmaras model was the only model that accurately predicted the asymmetric time-averaged wake topology, as reported in previous experimental and numerical studies, for the $\beta_e = 17.8°$ notchback Ahmed body at $Re = 5 \times 10^4$. The drag coefficient decreased with increasing Reynolds number, while the lift coefficient remained constant for $Re \geq 1 \times 10^4$. The wake structure exhibited three regimes: symmetric ($Re \leq 1 \times 10^4$), transitionally asymmetric ($1 \times 10^4 < Re \leq 3.5 \times 10^4$) and fully asymmetric ($Re > 3.5 \times 10^4$) states. The wake asymmetry was attributed to an imbalance in entrainment from the sides and asymmetric separation from the roof and the C-pillars of the body. The tilting and stretching terms in the vorticity transport equation were used to provide insight into the source of asymmetry in the vorticity field around the body.

Acknowledgments

I would like to express my sincere appreciation to my thesis advisor, Dr. Ebenezer Ekow Essel, whose unwavering support, guidance, and invaluable insights have been instrumental throughout this research journey in Concordia Turbulence Research Laboratory. Your mentorship and dedication to fostering intellectual growth have profoundly shaped this work.

I am also grateful to Dr. Kadem, Dr. Ng, and Dr. Roberdet for graciously agreeing to serve on my thesis defense committee.

My heartfelt thanks extend to my labmates Liam, Hung, Akili, Ashim and Joseph for their assistance, encouragement, and valuable discussions that have enriched the development of this thesis.

Lastly, I extend my deepest gratitude to my family and friends and fiancée for their unwavering encouragement, patience, and understanding throughout this academic pursuit. Their continuous support has been a constant source of strength.

This work would not have been possible without the collective contributions and encouragement of all those mentioned above.

Contents

List of figures

List of tables

List of acronyms

BR	Blockage Ratio
CFD	Computational Fluid Dynamics
DNS	Direct Numerical Simulation
EB	Elliptic Blending
EV	Eddy Viscosity
HRe SA	High Re Spalart-Allmaras
IDDES	Improved Delayed Detached Eddy Simulations
LES	Large Eddy Simulations
LPS 2L	Linear Pressure Strain Two-Layer
PANS	Partially Averaged Navier-Stokes
QPS	Quadratic Pressure Strain
RANS	Reynolds Averaged Navier-Stokes
RKE 2L	Realizable k-epsilon Two-Layer
RSB	Reflectional Symmetry-Breaking
SA	Spalart-Allmaras
SKO	Standard k-omega
SMC	Second Moment Closure
SSA	Standard Spalart-Allmaras
SSTKO	SST k-omega
URANS	Unsteady Reynolds Averaged Navier-Stokes
V2F	V2F k-epsilon

Nomenclature

A	area of the reverse flow region
D	Reynolds stress diffusion

C_D	drag coefficient
C_L	lift coefficient
C_f	skin friction coefficient
C_p	pressure coefficient
C_μ	model coefficient
$C_{\varepsilon 1}$	model coefficient
$C_{\varepsilon 2}$	model coefficient
$C_{\varepsilon 3}$	model coefficient
C_{1s}	model coefficient
C_3	model coefficient
C_{3s}	model coefficient
C_{s1}	model coefficient
C_{s2}	model coefficient
C_{r1}	model coefficient
C_{r2}	model coefficient
C_{r3}	model coefficient
C_{r3}^*	model coefficient
C_{r4}	model coefficient
d_{y_2}	wall-normal distance, mm
d_{y_1}	wall-normal distance, mm
d_z	spanwise distance, mm
$\boldsymbol{f}_b$	resultant of the body forces
F_2	blending function
f_{v1}	damping function
f_μ	damping function
G	ground clearance
h	height of the body
h_D	height of the body deck

$\mathbf{I}$	identity tensor
L	length of the body
L_D	length of the body deck
L_S	length of the body roof
L_r	length of the reverse flow behind the trunk
$\bar{p}$	mean pressure
P_k	production term
P_ε	production term
Q	Q_criterion
Re	Reynolds number
$\mathbf{R}$	Reynolds stress tensor
R	radius of rounding
$\mathbf{S}$	mean strain rate tensor
$\mathbf{S_R}$	user-specified source term
S_x	streamwise stretching
S_y	wall-normal stretching
S_z	spanwise stretching
S_k	source term
S_ε	source term
$\overline{\mathbf{T}}$	mean viscous stress tensor
$\mathbf{T}_{RANS}$	stress tensor
T_x	streamwise tilting
T_y	wall-normal tilting
T_z	spanwise tilting
T	turbulent time scale
U	streamwise mean velocity
U_∞	freestream velocity
U_τ	friction velocity
$\overline{\mathbf{V}}$	mean velocity

V_b	volume of the reverse flow behind the back
V_{s-d}	volume of the reverse flow on the slant-deck
V	wall-normal mean velocity
W	width of the body
z_g	spanwise barycenter of the reverse flow region
dx, dy, dz	vector spacing
k	turbulence kinetic energy
x, y, z	coordinates
$\partial C_{pb}/\partial z$	gradient of the pressure coefficient on the back
$\partial C_{pd}/\partial z$	gradient of the pressure coefficient on the deck
$\partial C_{ps}/\partial z$	gradient of the pressure coefficient on the slant
β	backlight angle
β_e	effective backlight angle
Ω_x	streamwise vorticity
Ω_y	wall-normal vorticity
Ω_z	spanwise vorticity
ε	dissipation rate
ε_0	ambient turbulence value
$\underline{\phi_s}$	slow pressure strain term
$\underline{\phi_r}$	rapid pressure-strain term
$\underline{\phi_{1w}}$	slow wall-reflection term
$\underline{\phi_{2w}}$	rapid wall reflection term
δ_ν	viscous length scale
μ_{air}	dynamic viscosity of air
μ_t	turbulent eddy viscosity
ν	kinematic viscosity
$\tilde{\nu}$	modified diffusivity
ω	specific dissipation rate

ρ	density
ρ_{air}	density of air
τ_w	wall shear stress
Γ_x	streamwise tilting/stretching
Γ_y	wall-normal tilting/stretching
Γ_z	span-wise tilting/stretching

Chapter 1

Introduction

1.2 Motivation

Currently, addressing climate change and reducing greenhouse gas (GHG) emissions have become a critical sustainability goal. The Paris Agreement, adopted by 196 nations, including Canada during the UN Climate Change Conference (COP21) in 2015, addresses this unified goal. As the world collectively strives for eco-friendly technologies, the need for innovative solutions across various industries becomes increasingly important. Sustainable practices are no longer a mere option but a necessity for the preservation of our planet.

Ground transportation is a major contributor to GHG emissions and climate change, primarily due to the effects of aerodynamic drag on fuel consumption. Therefore, reducing the aerodynamic drag of ground vehicles is highly important within the transportation industry. With the rapid global emergence of eco-friendly vehicles, such as electric and hydrogen vehicles, minimizing aerodynamic drag becomes even more vital for optimizing their driving range, reducing range anxiety, and increasing market acceptance. Consequently, there is a strong need to enhance our understanding of the generation mechanism of aerodynamic drag of ground vehicles to develop cost-effective flow control strategies aimed at improving their energy efficiency.

The flow around ground vehicles has been studied over the past decade using both experimental and numerical methods. For a ground vehicle, the fore-end experiences a high-pressure due to the stagnation of the approach velocity that directly incident the vehicle. Flow may

separate from the front leading edge and reattached on the sides and root of the body followed by boundary layers growth on the surfaces as the flow past the body. The flow separates at the rear end of the body which generates a highly three-dimensional (3-D) low-pressure wake region. The difference in pressure between the front and the rear end is found to account for about 80% of the total drag experienced by ground vehicles (Ahmed et al., 1984). As experiments on full-scale vehicles can be complex to set up and test, simplified models of vehicle are often used to study the flow around ground vehicles. Examples of simplified models used include the Lorry model (Dalla Longa et al., 2019), the Windsor model (Pavia et al., 2018) and the Ahmed body (Ahmed et al., 1984). The Ahmed body is used in the present study.

1.2 Literature review

The Ahmed body (Ahmed et al., 1984) is a simplified vehicle model often used to study the wake characteristics and aerodynamic properties of ground vehicles. The model consists of rounded fore-end, a rectangular mid-section and rear-end that can be modified as a hatchback (Ahmed et al., 1984), square-back (Grandemange et al., 2012), notchback (Sims-Williams et al., 2011) (see Figure 1.1). A literature review of the different configurations of Ahmed body is proposed in this section.

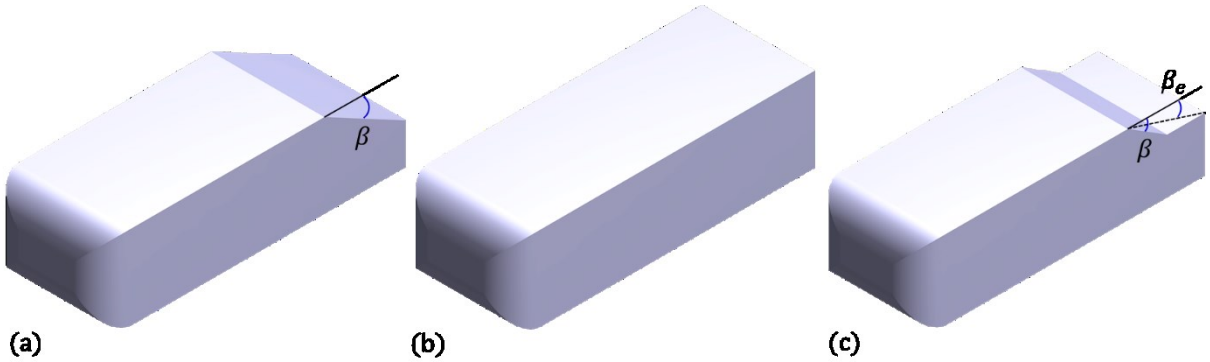

Figure 1.1: Representation of (a) hatchback, (b) square-back, and (c) notchback Ahmed body with the nomenclature.

1.2.1 Hatchback Ahmed body

The original Ahmed body, often referred to as hatchback Ahmed body was first proposed by Ahmed et al., (1984) to study the flow around vehicles with a similar shape such as sport utility vehicles. The geometry was designed to generate the salient flow features around ground vehicles, excluding detailed effects such as wheels. The model generates a prominent 3-D flow displacement in the front with a relatively uniform flow in the middle section followed by a large and structured wake behind the body. The original Ahmed body is 1044 mm long, 389 mm wide and has a height of 288 mm. The model is composed of three parts: a fore body, a mid section, and a rear end. To mitigate any possible flow separation from the front of the body, the edges of the front are rounded with a radius of 100 mm. The interchangeable rear end integrates a slant (see Figure 1.1a) with backlight angle, $\beta \in [0°, 40°]$.

Using wind tunnel at $Re = U_\infty h/\nu = 1.2 \times 10^6$ Ahmed et al., (1984) found that the front-end contribution to the pressure drag was the same for all tested slant angles excluding that of $\beta = 30°$ suggesting a weak interaction between the front and the rear end of the body. It was also shown that most of the drag ($\sim 85\%$) generated by the body is due to pressure drag from the rear end. The wake structure behind the Ahmed body is very complex and includes a separation region on the slant, counter-rotating vortices emanating from the C-pillars and a recirculation torus behind the back. The strength of the C-pillar vortices is sensitive to the slant angle, and the recirculation torus is composed of two vertically aligned recirculation bubbles (Ahmed et al., 1984; Strachan et al., 2007; Vino et al., 2005). The slant angle $\beta = 30°$ was identified as a critical angle for the highest drag coefficient. The flow topology is classified into three main regimes depending on the slant angle. For Regime I ($\beta \leq 12.5°$), the separated flow from the trailing edge of the roof fully attaches to the slant with a weak pair of longitudinal vortices in the near wake region, resulting in

an aerodynamic drag coefficient (C_D) of $C_D \approx 0.25$ (Strachan et al., 2007). In Regime II ($12.5° < \beta < 30°$), the longitudinal vortices are stronger compared to that of Regime I. The separated flow from the roof reattaches on the slanted surface forming a recirculation bubble. The drag coefficient increases with backlight angle (Vino et al., 2005). For Regime III $\beta > 30°$, the separated flow from the roof fails to reattach on the slanted surface, resulting in a fully separated flow at the rear-end of the body. The drag coefficient suddenly decreases while the C-pillar vortices are significantly weakened. Regime I and Regime III are usually referred to as the low-drag regimes, while Regime II is known as high-drag regime. After the pioneering work of Ahmed et al., (1984), the model has been used extensively both experimentally and numerically to enhance physical insight on the flow around the ground vehicles (Gilliéron & Kourta, 2013; Krajnović & Davidson, 2005a; Rouméas et al., 2009). For example, using large eddy simulation, Krajnović & Davidson, (2005a) observed additional pair of counter-rotating vortices generated near the bottom corners of the base for $\beta = 25°$. The elliptical Ahmed body is a modified version of the hatchback Ahmed body with the rear-end side edges rounded to display an elliptical shape (Siddiqui & Agelin-Chaab, 2022). Investigations using a slant angle, $\beta = 25°$ showed a reorientation of the recirculation bubbles compared to the standard hatchback. As a result, the elliptical geometry shifted the flow regime of the $\beta = 25°$ from high-drag to a low-drag regime when compared to the standard hatchback model.

1.2.2 Square-back Ahmed body

The square-back Ahmed body is a configuration of the original Ahmed body displaying a flat back obtained by setting the slant angle to zero ($\beta = 0°$) as shown in Figure 1.1b. In contrast to the hatchback Ahmed body, the square-back Ahmed body has only recirculation bubbles behind the vertical base of the body, yet its wake dynamics is complex mainly due to vortex shedding.

This geometry has gained in popularity within the research community since Grandemange et al., (2012) documented and characterized a bi-modal wake behaviour observed on the model. The bi-modality is found to have timescales, $T_s \sim 10^3 h/U_\infty$, where h is the height of the body and U_∞ is the freestream velocity and is characterized by random shift of the reverse flow region between two reflectional symmetry-breaking (RSB) positions. The RSB positions are found to be mutually symmetric with respect to the vertical symmetry plane resulting in a symmetric time-averaged wake. Low Reynolds number studies on the square-back Ahmed body suggested that the bi-modality behaviour appeared after a critical Reynolds number of $Re \sim 365$ in the laminar region (Grandemange et al., 2012). However, the bi-modality is found to be independent of the Reynolds number in the turbulent region (Fan et al., 2020).

Further investigations by Grandemange et al., (2013a) show that the bi-modality is dependent on the ground clearance (G/h where G denotes underbody gap) and the aspect ratio of the body (W/h with W the width of the model). Three regimes were identified depending on the ground clearance: low ground clearance ratio ($G/h < 0.07$), moderate ground clearance ratio ($0.07 \leq G/h \leq 0.12$) and high ground clearance ratio ($G/h > 0.12$). For low G/h, only one recirculation bubble is formed behind the back of the body due to the viscous effects on the ground and no sign of bi-modality was observed. Previous investigations from Bonnavion & Cadot, (2018) and Haffner et al., (2020) also demonstrate a suppression of the bi-modality due to yaw and pitch angle. As the ground clearance ratio rises into the moderate regime, the viscous effects gradually diminish, and the flow become more energetic and exits the gap as a jet-like upwash flow. Two recirculation bubbles are generated behind the body as the upwash from the ground clearance clashes with the downwash from the top of the body. Additional recirculation bubble is also generated on the ground, as part of the upwash attaches to the ground due to a severe adverse

pressure gradient in the vicinity. These configurations typically result in low base pressure, which consequently lead to high drag. For high ground clearance ratios, the flow separation on the ground is suppressed due to a more energetic upwash from the underbody. A pair of recirculation bubbles is formed behind the back, which is associated with the torus (Krajnović & Davidson, 2004; Lucas et al., 2017). In contrast to the low ground clearance ratio, which was found to suppress the bi-modality, both moderate and high ground clearance ratio ($G/h \geq 0.07$) displayed bi-modality behaviour. In terms of the aspect ratio, only the direction of the bi-modality was altered. When $W/h > 1$ the bi-modality occurs in the spanwise direction while the wall-normal direction is selected when $W/h < 1$.

Numerical simulations based on unsteady Reynolds-averaged Navier-Stokes (URANS) (Khalighi et al., 2012), partially averaged Navier-Stokes (PANS) (Rao et al., 2018), detached eddy simulations (DES) (Guilmineau et al., 2018), improved delayed detached eddy simulations (IDDES) (Fan et al., 2020; Kang et al., 2021) and large eddy simulations (LES) (Dalla Longa et al., 2019) have been used to study the flow past square-back Ahmed body. Dalla Longa et al., (2019) showed that the shedding of large hairpin vortex structures from the upper edge of the back surface induces the bi-modality behaviour. A second timescale, $T_s \sim 5h/U_\infty$ was also observed in the wake of the square-back Ahmed body and was associated with weak coherent oscillations in the vertical and lateral directions (Grandemange, Gohlke, et al., 2013b; Plumejeau et al., 2020). The reverse flow region was found to undergo a quasi-periodic expansion and contraction, referred to as pumping motion, with a normalised frequency $fh/U_\infty = 0.08$ (Volpe et al., 2015).

Recent studies on hatchback and square-back Ahmed body examine the effects of passive and active flow control strategies on the wake topology, aimed at reducing aerodynamic drag. Examples of active control strategies implemented on the Ahmed bodies include steady (Zhang et

al., 2018), pulsed blowing (Joseph et al., 2013), steady suction (Roumeas et al., 2009), alternate steady blowing and suction (Bruneau et al., 2011), plasma actuator (Kim et al., 2020), and synthetic jet (Tounsi et al., 2016). Examples of passive control strategies include vertical splitter plates (Gilliéron & Kourta, 2010), straight and inward slanted cavities (Grandemange et al., 2015; Lucas et al., 2017), boat tail and flaps (Grandemange, Mary, et al., 2013; Khalighi et al., 2012). For the high-drag hatchback Ahmed body ($\beta = 25°$), a maximum reduction in drag coefficient of 29% was obtained with the use of steady blowing on the base side, top and bottom edges (Zhang et al., 2018). On the other end, a reduction of 4% was achieved using combined steady suction and blowing for a $\beta = 35°$ model (i.e., low drag model) (Jahanmiri & Abbaspour, 2011). For square-back Ahmed body, the boat tail behind the base was found to be the most efficient with a maximum drag reduction of 31% (Verzicco et al., 2002) and for the active flow control techniques, the steady produced the best results with 24% of drag reduction (C. H. Bruneau et al., 2010). A detailed review of the flow control strategies for hatchback and square-back Ahmed body is available in Yu & Bingfu, (2021).

1.2.3 Notchback Ahmed body

The notchback Ahmed body, which best mimics sedans, is an Ahmed body with a trunk behind the back surface (see Figure 1.1c). It possesses all three features displayed by the standard Ahmed body with additional complexity introduced by the presence of the trunk.

Sims-Williams et al., (2011) used surface flow visualisation, force measurement, multi-hole probe, particle image velocimetry, and RANS to perform a comprehensive investigation of flow around the notchback Ahmed body using sixteen different rear-end configurations. The effects of backlight ($\beta \in [17.8°–90.0°]$) and effective backlight angle ($\beta_e \in [17.8°–31.8°]$) (Figure 1.1c) were examined at Reynolds number, $Re = 5 \times 10^5$. Three wake topologies were observed: fully

separated, reattaching symmetric and reattaching asymmetric. For $\beta \leq 42°$ the flow separates from the trailing edge of the roof and reattaches either on the slant or the trunk with a symmetric or an asymmetric wake topology. Particularly, for $\beta = 42.0°$ & $\beta_e = 21.0°$ the wake was found to be symmetric while for $\beta = 31.8°$ & $\beta_e = 17.8°$ the flow was asymmetric. Different levels of asymmetry were observed suggesting the asymmetry depends on β and β_e. In contrast, for $\beta > 42°$, the separated flow from the roof trailing edge fails to reattach on the slant-deck region with no sign of asymmetry. For low effective backlight angle ($\beta < 25.3$), the drag coefficient increases as the effective backlight angle increases until $\beta_e = 25.3°$ which is also found to be the transitioning angle between reattached $\beta_e < 25.3°$ and fully separated $\beta_e \geq 25.3°$ flow. Above that critical angle, the drag reduces and is comparable to that of square-back Ahmed body for similar test conditions.

Following insights from Sims-Williams et al., (2011), He et al., (2021a) performed a LES study on notchback Ahmed body with $\beta_e = 17.8°$ and $21.0°$ at $Re = 5 \times 10^4$. They used the gradients of the pressure coefficient on the slant, deck and back to characterise the flow topology of the body and found that for $\beta_e = 21.0°$, the wake behind the body displayed a stable symmetric state, while for $\beta_e = 17.8°$, a random switch of two stable asymmetric mirrored states is observed similar to the bi-modality of the square-back Ahmed body. The wake asymmetry was attributed to an asymmetric separation of the flow from the roof trailing edge and the switching to the opposite stable asymmetric state appeared to be initiated by the deflection of vortices from the trailing edges. He et al., (2021c) also investigated the effects of the blockage ratio ($BR = 0, 5, 10$ and 20%) on the asymmetric wake of the $\beta_e = 17.8°$ notchback Ahmed body. They found that the wake remains asymmetric for $BR \leq 10\%$, but the effect of blockage ratio was negligible for $BR \leq 5\%$. He et al., (2021d) investigated the effects of rounding the roof trailing edge on the

wake of a $\beta_e = 17.8°$ notchback. Two geometries with the trailing edge rounded with radius $R_t = 0.28h$ & $0.84h$ were compared to a baseline case with a sharp edge. The investigations were performed for $Re \in [5 \times 10^4, 25 \times 10^4]$. For each Reynolds number, the wake of the baseline was bi-stable with a high frequency switching for the highest Re which tends to depict a symmetric time-averaged flow structure. For the rounded edges, the wake topology was highly dependent on the Reynolds number. Especially, for $R_t = 0.28h$ the wake was asymmetric for $Re = 5 \times 10^4$, but symmetric for $Re = [7.5 \times 10^4, 15.0 \times 10^4]$ and returned to an asymmetric state for $Re \geq 17.5 \times 10^4$. In contrast to $R_t = 0.28h$, $R_t = 0.84h$ showed a symmetric wake at $Re = 5 \times 10^4$. The symmetric wake topology was attributed to the lack of separated flow over slanted surface, which reduced the drag and lift coefficients. He et al., (2022a) also showed that, for the baseline case, the time history of the gradient of the pressure coefficient depicted a tri-stable behavior for $Re = [12.5 \times 10^4, 17.5 \times 10^4]$ with a symmetric behavior for $Re > 20 \times 10^4$. For the highest Re, the symmetric state was found to be unstable as introducing small yaw angles shifted the regime to an asymmetric state.

1.3 Objective

As depicted by §1.2.1, §1.2.2, and §1.2.3, compared to the hatchback and square-back Ahmed body, the notchback Ahmed body has received less attention. Furthermore, past investigations on the notchback Ahmed body mostly focussed on high Reynolds numbers ($Re \geq 5 \times 10^4$) leaving a gap in our understanding of the flow around such body for low Reynolds numbers. Therefore, the objective of the present study is to investigate the flow characteristics of the notchback Ahmed body with effective backlight angle, $\beta_e = 17.8°$ subjected to wide range of low ($Re = 5 \times 10^3$) to high Reynolds numbers ($Re = 5 \times 10^4$). Despite the increasing popularity of LES and hybrid RANS-LES, the RANS framework remains a predominant choice in industrial computational fluid

dynamics (CFD) (Klein et al., 2015) especially when dealing with parametric investigations, due to computational cost. However, given the inherent limitations of RANS in predicting such complex turbulent flow with wake asymmetry, detailed turbulence model assessments are required to choose a model that satisfactorily predicts the wake characteristics from an experiment or LES. Therefore, before studying the effects of the Reynolds number on the wake characteristics of the Ahmed body, RANS model assessment was performed using nine (9) models consisting of six eddy viscosity and three second moment closure models. The simulations were performed at $Re = 5 \times 10^4$ and results were validated with the LES of He et al., (2021b). The model that satisfactorily simulated the salient flow features was selected for the Reynolds number investigation.

1.4 Organisation

The thesis comprises four chapters, each summarized as follows:

Chapter 1 is a general introduction presenting the motivation of the thesis and giving a brief literature review on three main Ahmed body models. The objective and the outline of the thesis are also presented there.

Chapter 2 presents fundamental equations of fluid mechanics important for CFD simulations and a brief introduction to the turbulence models used in the present study.

Chapter 3 presents the investigation of the wake characteristics of a notchback Ahmed body subjected to ten Reynolds numbers ranging from $Re = 5 \times 10^3$ to $Re = 5 \times 10^4$. The numerical setup is introduced here, as well as a detailed turbulence models assessment validated against time-averaged LES results reported in He et al., (2021b). Mean velocities and vorticities, skin friction, drag and lift coefficients, and the tilting and stretching terms of the transport equation of the mean

vorticity are used to provide an in-depth discussion on the effects of the Reynolds number on the wake characteristics of the notchback Ahmed body.

Chapter 4 includes a conclusion summarizing the key findings and insights drawn from the investigation. Additionally, it offers recommendations for potential future work.

Chapter 2

In this chapter, the laws of conservation of mass and conservation of momentum are introduced. A brief overview of the different turbulence models used in the present study is also provided. A full description of the turbulence models is available in the STAR-CCM+ User Guide (Siemens Digital Industries Software, 2021).

Methodology

2.1 Governing equations

2.1.1 Conservation of mass

The law of conservation of mass, also known as the continuity equation, indicate that mass is neither created nor destroyed within a system or the time rate of change of the system mass is equal to zero. This is expressed as:

$$\frac{\mathrm{d}m}{\mathrm{d}t} = 0 \tag{2.1}$$

with m the system mass and t is time. Using the Reynolds transport theorem, Eq. 2.1 can be re-expressed as:

$$\frac{\mathrm{d}}{\mathrm{d}t}\int_{cv} \rho \, d\forall = \frac{\partial}{\partial t}\int_{cv} \rho \, d\forall + \int_{cs} \rho \boldsymbol{V} \cdot \hat{\boldsymbol{n}} \, dA = 0 \tag{2.2}$$

Time rate of change in mass of the system	=	Time rate of change of the mass content within the control volume (CV)	+	Net rate of flow of mass through the control system (CS)

where ρ is the density, $\boldsymbol{V}$ is the velocity vector and $\hat{\boldsymbol{n}}$ is the outward pointing normal vector to the control surface. Using the divergence theorem, the conservation of mass can also be expressed in differential form as:

$$\frac{\partial \rho}{\partial t} + \nabla \cdot (\rho \boldsymbol{V}) = 0 \tag{2.3}$$

2.1.2 Conservation of momentum

The conservation of momentum arises from Newton's second law of motion and states that the sum of forces acting on a body is equal to the time rate of change of its momentum (i.e., product of the mass and acceleration):

$$\Sigma \boldsymbol{F} = m\boldsymbol{a} = \frac{\mathrm{d}}{\mathrm{d}t}(m\boldsymbol{V}) \tag{2.4}$$

with $\boldsymbol{F}$ the applied forces and $\boldsymbol{a}$ the acceleration vector. The forces can be divided into two types: surface forces (pressure forces and viscous forces) and body forces (e.g., gravity force, Coriolis force and electromagnetic force). For the current study, all the body forces are ignored. The conservation of momentum is then given by:

$$\frac{\mathrm{d}}{\mathrm{dt}} \int_{cv} \rho \boldsymbol{V} \, d\forall + \int_{cs} \rho \boldsymbol{V} (\boldsymbol{V} \cdot \hat{\boldsymbol{n}}) \, dA = \int_{cs} -p \cdot \hat{\boldsymbol{n}} \, dA + \int_{cs} \tau \cdot \hat{\boldsymbol{n}} \, dA = 0 \tag{2.5}$$

with p the pressure and τ the viscous stress tensor defined as:

$$\tau = \mu(\boldsymbol{\nabla V} + (\boldsymbol{\nabla V})^{\mathrm{T}}) - \frac{2}{3}\mu(\boldsymbol{\nabla} \cdot \boldsymbol{V})\mathbf{I} \tag{2.6}$$

where μ is the dynamic viscosity and **I** the identity matrix. The conservation of momentum can be expressed in a differential form as:

$$\frac{\partial}{\partial t}(\rho \boldsymbol{V}) + \boldsymbol{\nabla} \cdot [\rho(\boldsymbol{V} \otimes \boldsymbol{V}) + p\mathbf{I} - \tau] = 0 \tag{2.7}$$

2.2 Turbulence modeling

2.2.1 Introduction

Most fluid flows in engineering applications exhibit irregular and fluctuating quantities. These fluctuations often occur at scales and frequencies that are computationally expensive to resolve accurately in time and space. Rather than employing Direct Numerical Simulation (DNS), which solves for the exact governing equations of turbulent flows, a more cost-effective approach involves solving for averaged or filtered quantities to describe the turbulence structures. Turbulence models offer various methods for modeling these structures. There is a common notion that turbulence models serve as approximations of the actual turbulence phenomena. The level of approximation within each model varies based on the specific characteristics of the flow. Turbulence models are often divided into two categories: Reynolds-Averaged Navier-Stokes (RANS) turbulence models and scale-resolving simulations (e.g., LES and hybrid LES-RANS). In contrast to the RANS models that are modeling the whole flow field, the scale-resolving simulations resolve the large scales of turbulence while the small-scale motions are modeled (see Figure 2.1). As a result, the RANS models, which are used in the present study, require less

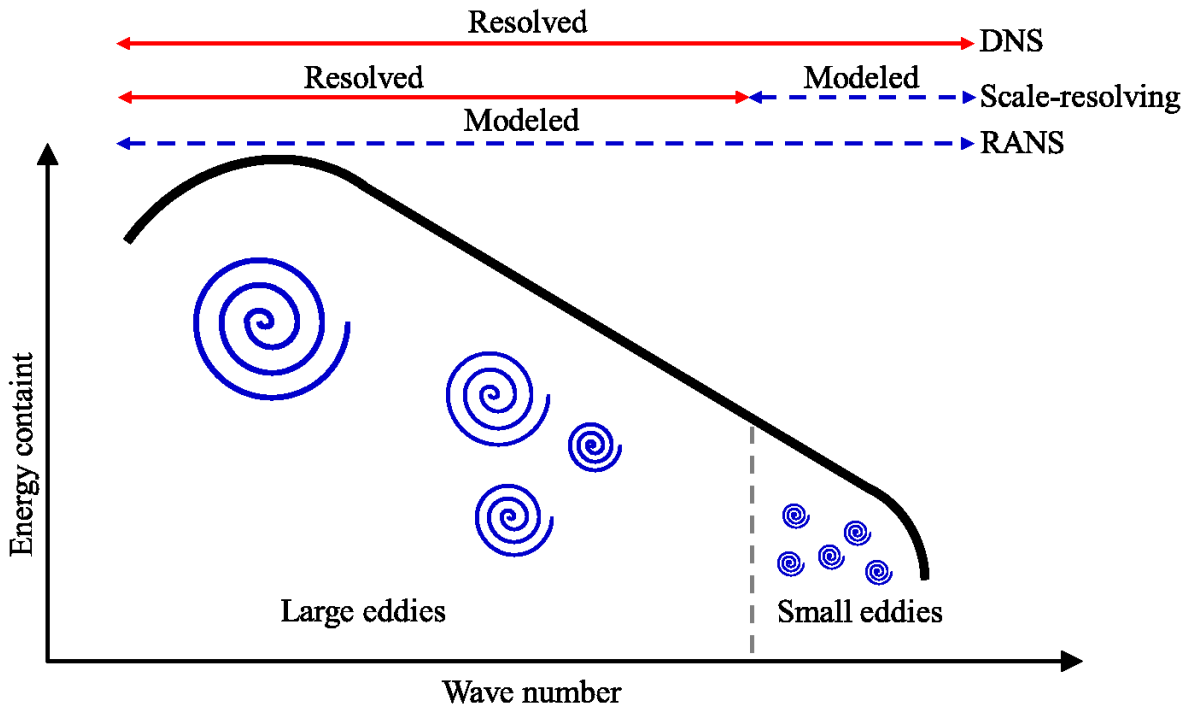

Figure 2.1: Energy cascade

computational resources compared to scale-resolving simulations or DNS. Here, the simulations are conducted using the commercial software STAR-CCM+ 2020, which employs finite volume method (FVM) to solve the RANS equations.

2.2.2 Reynolds Averaged Navier-Stokes equations

RANS modeling involves formulating a set of partial differential equations for describing turbulent flow features. These equations are derived from approximate versions of the Navier–Stokes equations. In the RANS equations, the process begins with decomposing flow variables into mean and fluctuating components (e.g. $u = U + u'$). The decomposed variables are inserted into the Navier–Stokes equations which are then averaged. For steady-state simulations and ignoring body forces, the resulting RANS equations are given as:

$$\nabla \cdot (\rho \overline{\mathbf{V}} \otimes \overline{\mathbf{V}}) = -\nabla \cdot \bar{p}\mathbf{I} + \nabla \cdot (\overline{\mathbf{T}} + \mathbf{T}_{RANS}) \tag{2.8}$$

with ρ, $\overline{\mathbf{V}}$, $\bar{p}$, $\mathbf{I}$, and $\overline{\mathbf{T}}$ representing the density, mean velocity, mean pressure, identity tensor, and the mean viscous stress tensor, respectively. The stress tensor $\mathbf{T}_{RANS}$ given as:

$$\mathbf{T}_{RANS} = -\rho\mathbf{R} + \frac{2}{3}\rho \mathrm{tr}(\mathbf{R})\mathbf{I} \tag{2.9}$$

where,

$$\mathbf{R} = \begin{pmatrix} \overline{u'u'} & \overline{u'v'} & \overline{u'w'} \\ \overline{u'u'} & \overline{v'v'} & \overline{v'w'} \\ \overline{u'w'} & \overline{v'w'} & \overline{w'w'} \end{pmatrix} \tag{2.10}$$

with $\frac{1}{2}\mathrm{tr}(\mathbf{R}) = k$, the turbulent kinetic energy. $\mathbf{T}_{RANS}$ represents an additional unknown term that requires modeling for closure of the RANS equations. Two main approaches are used to provide a closure by modelling $\mathbf{T}_{RANS}$: Eddy viscosity (EV) and Second Moment Closure (SMC) models. Taking advantage of the wide variety of models available in STAR-CCM+ and their predictive capabilities, six EV models and three SMC models were selected for the model assessment prior to performing the Reynolds number investigations of the flow around the notchback Ahmed body.

2.2.3 Eddy viscosity models

The eddy viscosity models are based on the Boussinesq assumption which presumes an analogy between the action of the viscous stresses and Reynolds stresses on the mean flow. Boussinesq proposed that the Reynolds stresses are proportional to the mean rates of deformation. The proportionality variable is the turbulent eddy viscosity, μ_t, and $\mathbf{T}_{RANS}$ is modelled as:

$$\mathbf{T}_{RANS} = 2\mu_t\mathbf{S} - \frac{2}{3}(\mu_t \nabla \cdot \overline{\mathbf{V}})\mathbf{I} \tag{2.11}$$

where $\mathbf{S} = 1/2(\nabla\overline{\mathbf{V}} + \nabla\overline{\mathbf{V}}^T)$, is the mean strain rate tensor. The challenge is now shifted from the Reynolds stresses to the modeling of the eddy viscosity term. This is achieved by solving additional transport equations, and the number of transport equations solved is used to categorize the EV model as a zero-equation, one-equation, or two-equation model. In this study, only one-equation and two-equation models are used and briefly discussed subsequently.

2.2.3.1 One-equation models

In order to solve for μ_t, the one-equation models solve for one additional transport equation. Here, the standard Spalart-Allmaras (SSA) and the high Re Spalart-Allmaras (HRe SA) models were selected. To determine the turbulent eddy viscosity, the SA model solves one transport equation for the modified diffusivity, $\tilde{\nu}$ (Spalart & Allmaras, 1992). In its standard form, the SA model is applied without wall functions and the entire turbulent boundary layer including the viscous sublayer is resolved. But for the high Reynolds number version (HRe SA), viscous damping within the buffer layer and viscous sublayer is not included. The turbulent eddy viscosity μ_t is calculated as:

$$\mu_t = \rho f_{v1} \tilde{\nu} \tag{2.12}$$

and the transport equation for the modified diffusivity $\tilde{\nu}$ is:

$$\nabla \cdot (\rho \tilde{\nu} \overline{\mathbf{V}}) = \frac{1}{\sigma_{\tilde{\nu}}} \nabla \cdot [(\mu + \rho \tilde{\nu}) \nabla \tilde{\nu}] + P_{\tilde{\nu}} + S_{\tilde{\nu}} \tag{2.13}$$

where f_{v1}, $\sigma_{\tilde{\nu}}$, $P_{\tilde{\nu}}$, and $S_{\tilde{\nu}}$ are the damping function, the model coefficient, the production term and user defined source term, respectively.

2.2.3.2 Two-equation models

The two-equation models solve for two additional transport equations for a velocity (V) and a length (L) scale, where $\mu_t = C\rho VL$ with C a coefficient. Here, four models were selected: the realizable k-epsilon two-layer (RKE 2L), V2F k-epsilon (V2F), standard k-omega (SKO) and SST k-omega (SSTKO) models. These models can be grouped as epsilon-based models (i.e., RKE 2L and V2F) and omega-based models (i.e., SKO and SSTKO). The turbulent kinetic energy (k) transport equation is solved to obtain the velocity scale, while the length scale is obtained by solving a transport equation for the rate of dissipation, ε for the epsilon-based models and the specific dissipation rate, $\omega \propto \varepsilon/k$ for the standard omega model. The SSTKO is a blended model of the two groups, where omega formulation is used close to the wall and epsilon formulation in the remaining flow field. The turbulent eddy viscosity for the epsilon-based model is calculated as:

$$\mu_t = \rho C_\mu f_\mu k T_e \tag{2.14}$$

where C_μ, f_μ, and T_e are the model coefficient, the damping function, and the turbulent time scale.

The RKE 2L model is an improved form of the standard k-epsilon model that combines the realizable k-epsilon model with the two-layer approach. The realizable k-epsilon uses a variable damping function f_μ and allows the model to satisfy constraints on the normal stresses consistent with the physics of turbulences (Shih et al., 1994). The two-layer approach suggested by (Rodi, 1991) allows k-epsilon models to be applied in the viscous layer. The computation is divided into two layers. In the viscous dominated near-wall flow region, ε is algebraically specified and is

blended smoothly with the value computed from solving the transport equation far from the wall. The transport equations for k and ε are:

$$\nabla \cdot (\rho k \overline{\mathbf{V}}) = \nabla \cdot \left[\left(\mu + \frac{\mu_t}{\sigma_k} \right) \nabla k \right] + P_k - \rho(\varepsilon - \varepsilon_0) + S_k \tag{2.15}$$

and,

$$\nabla \cdot (\rho \varepsilon \overline{\mathbf{V}}) = \nabla \cdot \left[\left(\mu + \frac{\mu_t}{\sigma_\varepsilon} \right) \nabla \varepsilon \right] + \frac{1}{T_e} C_{\varepsilon 1} P_\varepsilon - C_{\varepsilon 2} f_2 \rho \left(\frac{\varepsilon}{T_e} - \frac{\varepsilon_0}{T_0} \right) + S_\varepsilon \tag{2.16}$$

with σ_k, σ_ε, $C_{\varepsilon 1}$, and $C_{\varepsilon 2}$ model coefficients, P_k and P_ε production terms, $f_2 = \frac{k}{k+\sqrt{\nu\varepsilon}}$ the damping function and S_k and S_ε are user defined source terms. The term ε_0, is an ambient turbulence value which takes care of the turbulence decay and $T_0 = \max\left(\frac{k_0}{\varepsilon_0}, C_t \sqrt{\frac{\nu}{\varepsilon_0}} \right)$ is its attached time-scale with C_t a model constant (Jones & Launder, 1972).

In the case of the V2F model, in addition to solving the transport equations for k and ε, to compute μ_t, a wall-normal stress component $\overline{\vartheta^2}$ and an elliptic relaxation parameter f are also solved. The V2F model is designed such that it can handle wall effects in the turbulent boundary layers and accommodate non-local effects, thus it can capture the near-wall turbulence accurately, which is crucial to predict accurately skin friction and flow separation (Davidson et al., 2003; Durbin, 1996; Lien et al., 1998). The turbulent eddy viscosity μ_t is given as:

$$\mu_t = \rho \min\left(C_\mu k T, C_{\mu_{\vartheta^2}} \vartheta^2 T_S \right) \tag{2.17}$$

where $C_{\mu_{\vartheta^2}}$ is the model coefficient, T and T_S are turbulent time scale and limited time scale, respectively. The transport equations for k, ε, are similar to that of the standard k-epsilon model and the transport equations for $\overline{\vartheta^2}$ and f are given as:

$$\nabla \cdot \left(\rho \overline{\vartheta^2} \overline{\mathbf{V}}\right) = \nabla \cdot \left[\left(\mu + \frac{\mu_t}{\sigma_{\overline{\vartheta^2}}}\right) \nabla \overline{\vartheta^2}\right] + P_{\overline{\vartheta^2}} - \frac{6\rho \overline{\vartheta^2} \varepsilon}{k} \tag{2.18}$$

and,

$$\nabla \cdot (L^2 \nabla f) - f + P_f = 0 \tag{2.19}$$

where $P_{\overline{\vartheta^2}}$, $\sigma_{\overline{\vartheta^2}}$, and L are the production term, the model coefficient and a length scale, respectively.

The k-omega (Wilcox, 1998) model has an improved performance for boundary layers under adverse pressure gradients. In its original form, boundary layer computations are sensitive to the values of ω in the free-stream. This problem is not encountered by the k-epsilon models and was addressed in the SSTKO form using variable substitution to transform the ω transport equation into an ε transport equation. Here, the turbulent eddy viscosity is computed as:

$$\mu_t = \rho k T \tag{2.20}$$

where the turbulent time scale is calculated as $T = \alpha^*/\omega$ for SKO and $T = \min(\alpha^*/\omega, a_1/SF_2)$ for SSTKO, with $\alpha^*$and a_1 model coefficients, and F_2 is the blending function.

2.2.4 Second moment closure

The second moment closure models directly calculate the components of **R** (see Eq. 2.10) by solving their governing equations. Unlike the EV models, the SMC models account for the effects of turbulence anisotropy and high strain rates, and are usually expected to be more accurate for complex flow predictions. The transport equation for the Reynolds stress tensor **R** is given by:

$$\nabla \cdot (\rho \mathbf{R}\overline{\mathbf{V}}) = \nabla \cdot \mathbf{D} + \mathbf{P} + \mathbf{G} - \frac{2}{3}\mathbf{I}\Upsilon_M + \underline{\phi} - \rho\underline{\varepsilon} + \mathbf{S_R} \tag{2.21}$$

with **D, P, G,** Υ_M , $\underline{\phi}$, $\underline{\varepsilon}$, and $\mathbf{S_R}$ are the Reynolds stress diffusion, the turbulent production, the buoyancy production, the dilatation dissipation, the pressure strain tensor, the turbulent dissipation rate tensor, and a user-specified source, respectively (Speziale et al., 1991). The SMC models used in this study solve seven transport equations: six equations for the Reynolds stresses and one equation for the isotropic turbulent dissipation. Here, three models are used: Linear Pressure Strain Two-Layer (LPS 2L), Quadratic Pressure Strain (QPS), and Elliptic Blending (EB). For all the selected models,

$$\mathbf{D} = \mu\nabla\mathbf{R} + C_s\frac{k}{\varepsilon}(\mathbf{R}\cdot\nabla)\,\mathbf{R}, \tag{2.22}$$

$$\mathbf{P} = \rho(\mathbf{R}\cdot\nabla\overline{\mathbf{V}}^T + \nabla\overline{\mathbf{V}}\cdot\mathbf{R}), \tag{2.23}$$

and the turbulent dissipation rate is obtained solving:

$$\nabla \cdot (\rho\varepsilon\overline{\mathbf{V}}) = \nabla \cdot \left[\left(\mu + \frac{\mu_t}{\sigma_\varepsilon}\right)\nabla\varepsilon\right]\frac{\varepsilon}{k}\left[C_{\varepsilon 1}\left(\frac{1}{2}\mathrm{tr}(\mathbf{P}) + \frac{1}{2}C_{\varepsilon 3}\mathrm{tr}(\mathbf{G})\right) - C_{\varepsilon 2}\rho\varepsilon\right] \tag{2.24}$$

with the turbulent viscosity, $\mu_t = \frac{\rho C_\mu \left(\frac{1}{2} tr(\mathbf{R})\right)^2}{\varepsilon}$.

For the LPS 2L and QPS models, the turbulent dissipation term is used to solve for the turbulent dissipation rate tensor, $\underline{\varepsilon}$ as:

$$\underline{\varepsilon} = \frac{2}{3}\varepsilon \mathbf{I} \tag{2.25}$$

In the case of the EB model, the pressure-strain and dissipation terms are blended and modelled together as (Manceau & Hanjalić, 2002):

$$\underline{\phi} - \underline{\varepsilon} = (1-\alpha^3)\left(\underline{\phi}^w - \underline{\varepsilon}^w\right) + \alpha^3\left(\underline{\phi}^h - \underline{\varepsilon}^h\right) \tag{2.26}$$

with the couple $\underline{\phi}^w$and $\underline{\varepsilon}^w = \mathbf{R}\frac{\varepsilon}{k}$ and $\underline{\phi}^h$ and $\underline{\varepsilon}^h = \frac{2}{3}\varepsilon\mathbf{I}$, representing the pressure strain and dissipation terms in the near wall region and outer region, respectively. The blending parameter, α is solution to the elliptic equation $\alpha - L^2\nabla^2\alpha = 1$ where $L = 0.133\max\left(\frac{k^{\frac{3}{2}}}{\varepsilon}, 80\frac{\nu^{\frac{3}{4}}}{\varepsilon^{\frac{1}{4}}}\right)$ is the turbulent length scale.

The pressure strain terms for the EB model are given as:

$$\begin{aligned}\underline{\phi}^h = &-[C_1\rho\varepsilon + C_{1s}\mathrm{tr}(\mathbf{P}+\mathbf{G})]\mathbf{A} + \left(C_3 - C_{3s}\sqrt{\mathbf{A}:\mathbf{A}}\right)\rho k\mathbf{S} \\ &+C_4\rho k\left(\mathbf{S}\cdot\mathbf{A} + \mathbf{A}\cdot\mathbf{S} - \frac{2}{3}\mathbf{A}:\mathbf{SI}\right) + C_5\rho k(\mathbf{W}\cdot\mathbf{A} + \mathbf{A}\cdot\mathbf{W}^T)\end{aligned} \tag{2.27}$$

and,

$$\underline{\phi}^{w} = -5\rho\frac{\varepsilon}{k}\left[\mathbf{R}\cdot\mathbf{N}+\mathbf{N}\cdot\mathbf{R}-\frac{1}{2}\mathbf{R}\colon\mathbf{N}(\mathbf{N}+\mathbf{I})\right] \tag{2.28}$$

where, the anisotropy tensor, $\mathbf{A} = \frac{\mathbf{R}}{\mathrm{k}} - \frac{2}{3}\mathbf{I}$, the mean vorticity tensor $\mathbf{W} = 1/2(\nabla\overline{\mathbf{V}} + \nabla\overline{\mathbf{V}}^{T})$, and $\mathbf{N} = \left(\frac{\nabla\alpha}{\sqrt{\nabla\alpha\cdot\nabla\alpha}}\right)\otimes\left(\frac{\nabla\alpha}{\sqrt{\nabla\alpha\cdot\nabla\alpha}}\right)$.

For the QPS model, the pressure strain is modeled as (Speziale et al., 1991):

$$\begin{aligned}\underline{\phi} = -[C_{s1}\rho\varepsilon + C_{r4}\mathrm{tr}(\mathbf{P}+\mathbf{G})]\mathbf{A} + C_{s2}\rho\varepsilon\left(\mathbf{A}\cdot\mathbf{A}-\frac{1}{3}\mathbf{A}\colon\mathbf{A}\mathbf{I}\right) + \left(C_{r3}-C_{r3}^{*}\sqrt{\mathbf{A}\colon\mathbf{A}}\right)\rho k\mathbf{S} \\ + C_{r1}\rho k\left(\mathbf{A}\cdot\mathbf{S}+\mathbf{S}\cdot\mathbf{A}-\frac{\mathbf{2}}{\mathbf{3}}\mathbf{A}\colon\mathbf{S}\mathbf{I}\right) + C_{r2}\rho k(\mathbf{A}\cdot\mathbf{W}^{T}+\mathbf{W}\cdot\mathbf{A})\end{aligned} \tag{2.53}$$

where C_{s1}, C_{s2}, C_{r1}, C_{r2}, C_{r3}, C_{r3}^{*}, and C_{r4} are model coefficients available in STARCCM+ User Guide (Siemens Digital Industries Software, 2021).

For the LPS 2L model, the linear model of (Gibson & Launder, 1978) is used pressure strain is modelled as follows:

$$\underline{\phi} = \underline{\phi}_{s} + \underline{\phi}_{r} + \underline{\phi}_{1w} + \underline{\phi}_{2w} \tag{2.54}$$

where, $\underline{\phi}_{s}$, $\underline{\phi}_{r}$, $\underline{\phi}_{1w}$, and $\underline{\phi}_{2w}$ represent the slow pressure strain, rapid pressure-strain, slow wall-reflection, and rapid wall reflection terms, respectively.

Chapter 3

In this chapter, the effects of the Reynolds number on the wake characteristics of a $\beta_e = 17.8°$ notchback Ahmed body is provided. Prior to investigating the effect of the Reynolds number, a RANS model assessment is performed to select the model that satisfactorily reproduces results from previous investigations.

Effects of Reynolds number on the wake characteristics of a notchback Ahmed body

3.1 Introduction

Ground transportation is a major contributor to greenhouse gas emissions and climate change, primarily due to the effects of aerodynamic drag on fuel consumption. Therefore, reducing the aerodynamic drag of ground vehicles is a crucial sustainability goal within the transportation industry. With the rapid global emergence of eco-friendly vehicles, such as electric and hydrogen vehicles, minimizing aerodynamic drag becomes even more vital for optimizing their driving range, reducing range anxiety, and increasing market acceptance. Consequently, there is a strong need to enhance our understanding of the generation mechanism of aerodynamic drag of ground vehicles to develop cost-effective flow control strategies aimed at improving their energy efficiency.

The Ahmed body (Ahmed et al., 1984) is a simplified vehicle model often used to study the wake characteristics and aerodynamic properties of ground vehicles. The model consists of rounded fore-end, a rectangular mid-section and rear-end that can be modified as a hatchback,

square-back, notchback or elliptical-back (Figure 3.1) (Ahmed et al., 1984; Grandemange, Gohlke, et al., 2013b; Siddiqui & Agelin-Chaab, 2022; Sims-Williams et al., 2011). The wake structure of the generic hatchback Ahmed body exhibits three salient features: (i) a recirculation bubble on the rear slanted surface, (ii) a pair of counter-rotating longitudinal vortices emanating from the two slanted edges and (iii) recirculation bubbles behind the vertical base of the body (Ahmed et al., 1984; Krajnović & Davidson, 2005a, 2005b). The elliptical-back Ahmed body is akin to the hatchback, but the curvature of the rear-end alters the topology of the recirculation bubbles (Siddiqui & Agelin-Chaab, 2022). The square-back Ahmed body has only feature (iii) yet the wake dynamics is complex mainly due to the vortex shedding and the stochastic wake asymmetry, also known as bi-modality. The bi-modality is found to have timescales of order $10^3 h/U_\infty$, where h is the height of the body and U_∞ is the freestream velocity (Grandemange, Gohlke, et al., 2013b). The notchback Ahmed body, on the other hand, possesses all three features with additional complexity introduced by the presence of the trunk. However, the wake dynamics of the notchback Ahmed body, which best mimics sedans, are less understood compared to the well-studied hatchback and square-back Ahmed bodies.

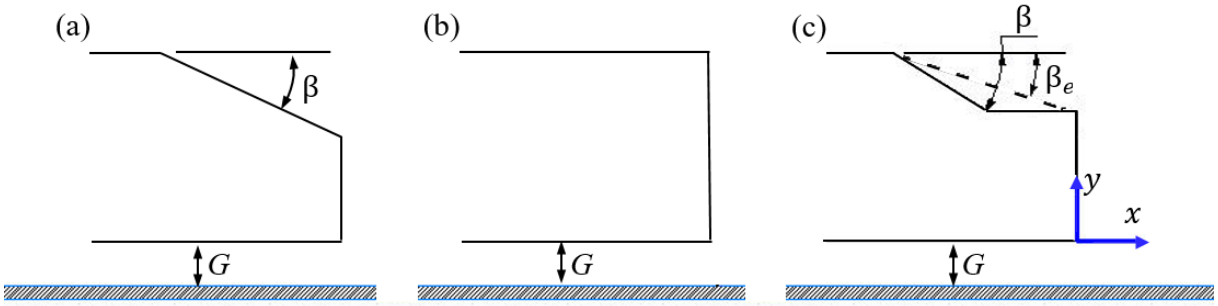

Figure 3.1: Schematic drawing of the rear end of (a) hatchback and elliptical-back, (b) square-back, and (c) notchback Ahmed body with the nomenclature.

A summary of previous studies that investigated the wake characteristics of the notchback Ahmed body is presented in Table 3.1 and the salient nomenclature is shown in Figure 3.1, where β is the backlight angle, β_e is the effective backlight angle and G is the ground clearance. Sims-Williams et al., (2011) investigated the effects of backlight ($\beta \in [17.8°–90.0°]$) and effective backlight ($\beta_e \in [17.8°–31.8°]$) angles on the wake structure of a notchback Ahmed body at Reynolds number, $Re = U_\infty h/\nu = 5 \times 10^5$, where ν is the kinematic viscosity. The experiments were conducted with surface flow visualization and augmented by three-dimensional (3D) numerical simulations using unsteady Reynolds Averaged Navier-Stokes (URANS) based on the Spalart-Allmaras turbulence model. Two main flow regimes were found based on the effective backlight angle: reattached flow ($\beta_e < 25.3°$) and fully separated flow ($\beta_e \geq 25.3°$). For the reattached flow regime, the separated flow from the roof reattaches to the slanted surface or the deck of the trunk, followed by separation at the trunk's trailing edge. As a result, a recirculation bubble is formed on the slanted surface and the deck, and a pair of counter-rotating bubbles behind the trunk. In the case of the fully separated flow regime, the separated flow from the roof fails to attach to the deck, forming a large recirculation bubble that spans from the slanted surface to the back of the trunk. The drag coefficient increases with increasing β_e in the reattached flow regime, but suddenly decreases in the fully separated regime. Sims-Williams et al., (2011) also found that within the reattached flow regime, the notchback Ahmed body exhibits symmetric wake topology at $\beta_e = 21.0°$ and asymmetric wake topology at $\beta_e = 17.8°$. The asymmetric wake structure has also been observed in previous flow visualization around a notchback car by Cogotti, (1987).

He et al., (2021a) conducted Large Eddy Simulation (LES) of the unsteady wake dynamics of the notchback Ahmed body at $Re = 5 \times 10^4$ and $\beta_e = 17.8°$ and $21.0°$ based on the experiments of Sims-Williams et al., (2011). They found that the asymmetric case ($\beta_e = 17.8°$) exhibits a

Table 3.1 Summary of previous studies on notchback Ahmed body

Authors	Technique	Re $(\times 10^4)$	$\beta(°)$	$\beta_e(°)$	G/h	C_D	BR (%)
Sims-Williams et al. (2011)	URANS & SFV	50	$17.8-90.0$	$17.8-31.8$	–	$0.30-0.40$	5.6
He et al. 2021a	LES, PT & HW	5	31.8 & 42.0	17.8 & 21.0	0.21	$0.32-0.35$	0, 2.2
He et al. 2021b	LES, IDDES & RANS	5	31.8 & 42.0	17.8 & 21.0	0.21	$0.32-0.33$	0
He et al. 2021c	LES	5	31.8	17.8	0.21	$0.34-0.62$	0, 5, 10, 20
He et al. 2021d; 2022a; 2022b	LES, PT & HW	$5-25$	31.8	17.8	0.21	$0.30-0.34$	0, 2.2

URANS: unsteady Reynolds Averaged Navier-Stokes, SFV: surface flow visualization, LES: large eddy simulation, PT: pressure taps, HW: hot wire, IDDES: improved delayed detached eddy simulation, BR: blockage ratio.

random wake bi-modality with long periods of left or right asymmetry. The asymmetry of the wake was attributed to asymmetric separation from the roof of the body and associated asymmetric reattachment on the deck. He et al., (2021c) investigated the effects of blockage ratio, $BR \in [0,20]\%$ on the bi-modality of the notchback Ahmed body ($\beta_e = 17.8°$) and found that the wake becomes symmetric when $BR > 10\%$. In He et al., (2021d), rounding the trailing edge of the roof was also observed to suppress wake bi-modality. He et al., (2022a) investigated the effects of high Reynolds numbers ($Re = 5 \times 10^4, 10 \times 10^4$ and 25×10^4) on the asymmetric state of the notchback Ahmed body ($\beta_e = 17.8°$) using LES and wind tunnel experiments. For $Re = 5 \times 10^4$, the wake exhibited bi-modality, but transitioned to a tri-stable state as the Reynolds number increased, due to the presence of an additional symmetric state.

As shown in Table 3.1, previous studies have examined the asymmetric wake characteristics of the $\beta_e = 17.8°$ notchback Ahmed body at high Reynolds numbers, $Re \geq 5 \times 10^4$. As a result, our understanding of wake characteristics at relatively low Reynolds numbers is limited. Such insights will guide the development of effective drag reduction strategies for a wide range of vehicle speeds. Therefore, the objective of the present study is to investigate the effects of Reynolds number, $Re \in [5 \times 10^3, 5 \times 10^4]$, on the wake dynamics of a notchback Ahmed body with $\beta_e = 17.8°$. Three-dimensional RANS is used to perform detailed study using ten different Reynolds numbers. A comprehensive evaluation of various turbulence models was first conducted to predict the asymmetric wake of the notchback Ahmed body at $Re = 5 \times 10^4$ and the results were validated against the LES results of He et al., (2021b). The turbulence models tested include two one-equation and four two-equation eddy viscosity (EV) models, as well as three second-moment closure (SMC) models. The model that satisfactorily reproduced the time-averaged LES results was then used to investigate the effects of Reynolds number. The remainder of this thesis

is organized as follows: §3.2 presents the numerical setup including the governing equations, turbulence models, computational domain, boundary conditions, grid independence test and model assessments. §3.3 presents the results and discussions while a summary of the major conclusion is provided in chapter 4.

3.2 Numerical setup

3.2.1 Governing equation

To perform the numerical simulations, the governing equations for RANS are discretized using the finite volume solver of STAR-CCM+ 2020. The software, STAR-CCM+ has been used in previous studies to investigate the wake characteristics of square-back (Fan et al., 2020; Kang et al., 2021) and notchback (He et al., 2021a, 2021b, 2021c, 2021d; He et al., 2022a, 2022b) Ahmed bodies with results that agree with experiments. For steady simulations neglecting body forces, the continuity equation is given as:

$$\nabla \cdot (\rho \overline{\boldsymbol{V}}) = 0 \tag{3.1}$$

and the RANS equation is:

$$\nabla \cdot (\rho \overline{\mathbf{V}} \otimes \overline{\mathbf{V}}) = -\nabla \cdot \bar{p}\mathbf{I} + \nabla \cdot (\overline{\mathbf{T}} + \mathbf{T}_{RANS}) \tag{3.2}$$

with ρ, $\overline{\mathbf{V}}$, $\bar{p}$, $\mathbf{I}$, and $\overline{\mathbf{T}}$ representing the density, the mean velocity, the mean pressure, the identity tensor, and the mean viscous stress tensor, respectively. The stress tensor, $\mathbf{T}_{RANS}$ given as:

$$\mathbf{T}_{RANS} = -\rho\mathbf{R} + \frac{2}{3}\rho k\mathbf{I} \tag{3.3}$$

where k is the turbulent kinetic energy and $\mathbf{R}$ is defined as

$$\mathbf{R} = \begin{pmatrix} \overline{u'u'} & \overline{u'v'} & \overline{u'w'} \\ \overline{u'u'} & \overline{v'v'} & \overline{v'w'} \\ \overline{u'w'} & \overline{v'w'} & \overline{w'w'} \end{pmatrix} \tag{3.4}$$

3.2.2 Turbulence models

Two main approaches can be used to model, $\mathbf{T}_{RANS}$ (Eq. (3.3)) to provide a closure of the RANS equations: Eddy Viscosity (EV) and Second Moment Closure (SMC) turbulence models. Based on preliminary assessment of the capabilities of turbulence models available in STAR-CCM+, six (6) EV models and three (3) SMC models were selected for detailed assessments and evaluations of the wake dynamics of the notchback Ahmed body. The EV models include two (2) one-equation models: standard Spalart-Allmaras model (denoted as SSA) and high Re Spalart-Allmaras (HRe SA) models, and four (4) two-equation models: realizable k-epsilon two-layer (RKE 2L), V2F k-epsilon (V2F), standard k-omega (SKO) and SST k-omega (SSTKO) models. The SMC models include Linear Pressure Strain Two-Layer (LPS 2L), Quadratic Pressure Strain (QPS), and Elliptic Blending (EB) models.

The EV models are based on the Boussinesq assumption, which relates the Reynolds stresses to the mean velocity gradients through the turbulent eddy viscosity, μ_t. As a result, the modelling effort is shifted from the Reynolds stresses to the eddy viscosity, where $\mathbf{T}_{RANS}$ is evaluated as

$$\mathbf{T}_{RANS} = 2\mu_t \mathbf{S} - \frac{2}{3}(\mu_t \nabla \cdot \overline{\mathbf{V}})\mathbf{I} \tag{3.5}$$

where $\mathbf{S} = 1/2(\nabla\overline{\mathbf{V}} + \nabla\overline{\mathbf{V}}^T)$, is the mean strain rate tensor. The Spalart-Allmaras (SA) models solve one transport equation for the modified diffusivity $\tilde{v}$, and μ_t is computed as

$$\mu_t = \rho f_{v1} \tilde{v} \tag{3.6}$$

where f_{v1} is a damping function. For the SSA, the turbulent boundary layer, including the viscous sublayer, is modeled without the use of wall functions. However, for the HRe SA model, wall functions are used and no damping function ($f_{v1} = 1$) (Eq. (3.6)) is used in the buffer and viscous sublayer. The SA models are computationally efficient and suitable for a wide range of engineering applications. The two-equation EV models solves two transport equations for velocity and length scales. All the two-equation EV models tested solves the turbulent kinetic energy, k to obtain the velocity scale. The ε −based models, (RKE 2L and V2F) solve the transport equation for turbulent dissipation rate, ε to obtain the length scale, while ω −based models (SKO) solve the transport equation for the specific dissipation rate, $\omega \propto \varepsilon/k$. The SSTKO solves a blended transport equation, which computes ω near the wall and ε further away from the wall. The turbulent eddy viscosity for ε −based models is usually evaluated as (Jones & Launder, 1972):

$$\mu_t = \rho C_\mu f_\mu k T \tag{3.7}$$

while, the equation for the ω −based models is given as

$$\mu_t = \rho k T \tag{3.8}$$

where $C_\mu = 0.09$ and f_μ are the model coefficient and the damping function, respectively. The turbulent time scale is calculated as, $\mathrm{T} = k/\varepsilon$ for RKE 2L and V2F, $\mathrm{T} = \alpha^*/\omega$ for SKO and T =

$\min(\alpha^*/\omega, a_1/SF_2)$ for SSTKO, where $\alpha^*$and a_1 are model coefficients, $S = |\mathbf{S}|$ and F_2 is the blending function.

In contrast to the EV models, the SMC models account for the individual Reynolds stresses without assuming turbulence isotropy. The selected SMC models solve six transport equations for the Reynolds stresses and one equation for the isotropic turbulent dissipation (ε). In terms of wall treatments, the ε −based models use scalable wall-functions to compute the turbulence quantities in the viscous sublayer, therefore less sensitive to grid refinement near the wall. The resolvable velocity of the ε −based models is usually above, $y^+ = 11.06$, where ($^+$) denotes scaling with U_τ and the viscous length scale, $\delta_\nu = \nu/U_\tau$ (Grotjans & Menter, 1998; Launder & Spalding, 1974). On the other hand, the ω −based models use low-Reynolds number near-wall expressions for ω in the viscous sublayer. This wall treatment requires finer grid spacing near the wall, with the recommended closest grid size specified as $y^+ \leq 1$. Detailed information about the specific transport equations and associated functions for each of the models is available in STAR-CCM+ User Guide (Siemens Digital Industries Software, 2021).

3.2.3 Computational domain, boundary conditions and test conditions

A scaled-down (1:4) of the original Ahmed body was used for the numerical simulation. The model has a height, $h = 72\text{mm}$, width, $W = 1.35h$ and length, $L = 3.82h$ and a rounded fore-end with radius, $R = 0.347h$ (Figure 3.2). The notchback rear-end has a trunk of height, $h_D = 0.687h$ and length, $L_D = 0.469h$ with a backlight and effective backlight $\beta = 31.8°$ and $\beta_e = 17.8°$, respectively, resulting in a roof length, $L_S = 2.847h$. The $\beta_e = 17.8°$ was chosen because previous studies (He et al., 2021a; Sims-Williams et al., 2011) have shown that the wake is

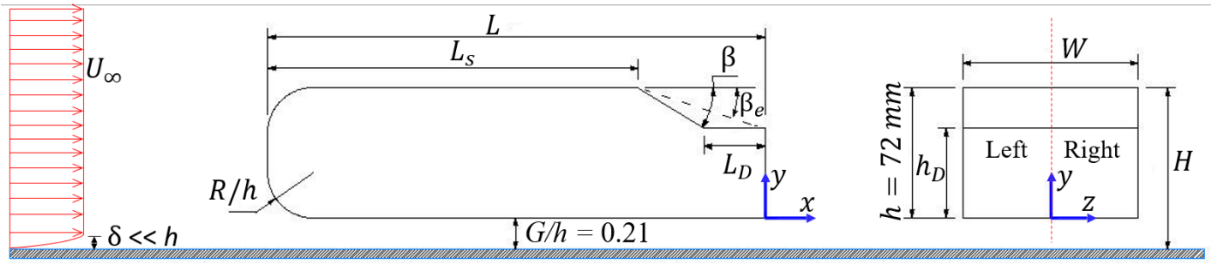

Figure 3.2: Schematic drawing of the notchback Ahmed body with the nomenclature used in the present study. The Ahmed body is placed in a uniform approach flow ($\delta \ll h$).

asymmetric for $Re \geq 5 \times 10^4$. Similar to He et al., (2021a), the ground clearance was fixed at, $G = 0.21h$. As shown in Figure 3.2, the left-handed Cartesian coordinate system is adopted here with the origin located at the midpoint of the lower edge of the back end of the model.

Figure 3.3(a-d) shows the computational domain used for the simulation. The origin of the coordinate system was set to coincide with the mid-span ($z = 0$) of the domain which has a height of $4.0h$ and a width of $10.0h$. The domain spanned a length of $30.8h$, with a streamwise distance of $8.0h$ from the inlet to the front of the body and a distance of $19.0h$ from the back end (i.e., base) to the domain outlet. Air at $25°C$ with a density of $\rho_{air} = 997.56\ \text{kg m}^{-3}$ and a dynamic viscosity of $\mu_{air} = 8.89\ \text{Pa s}^{-1}$ was used as a working fluid for the simulation. In terms of boundary conditions, the ground and the walls of the Ahmed body were set as no-slip condition while the roof of the domain and the side surfaces were set as symmetry planes. Dirichlet boundary conditions of uniform velocity, U_∞ and constant pressure outlet were assigned to the inlet and outlet of the domain, respectively. The inlet velocity was varied from $U_\infty = 1.08\ \text{m s}^{-1}$ to $10.87\ \text{m s}^{-1}$ to obtain ten (10) different Reynolds numbers with a wide range of $Re = 5 \times 10^3$ to $Re = 5 \times 10^4$ at an interval of 5000. The governing equations are discretized using a 2nd order upwind scheme and the system of algebraic equation resulting from the discretization was solved using a segregated algorithm where the conservation equations of mass and momentum in a sequential manner. For each simulation, the solution was considered converged when the root-

mean-square of the normalized residuals of the discretized equations was less 10^{-9} and the monitored averaged quantities, (e.g., drag coefficient (C_D) and lift coefficient (C_L)) are independent of accumulated timestep.

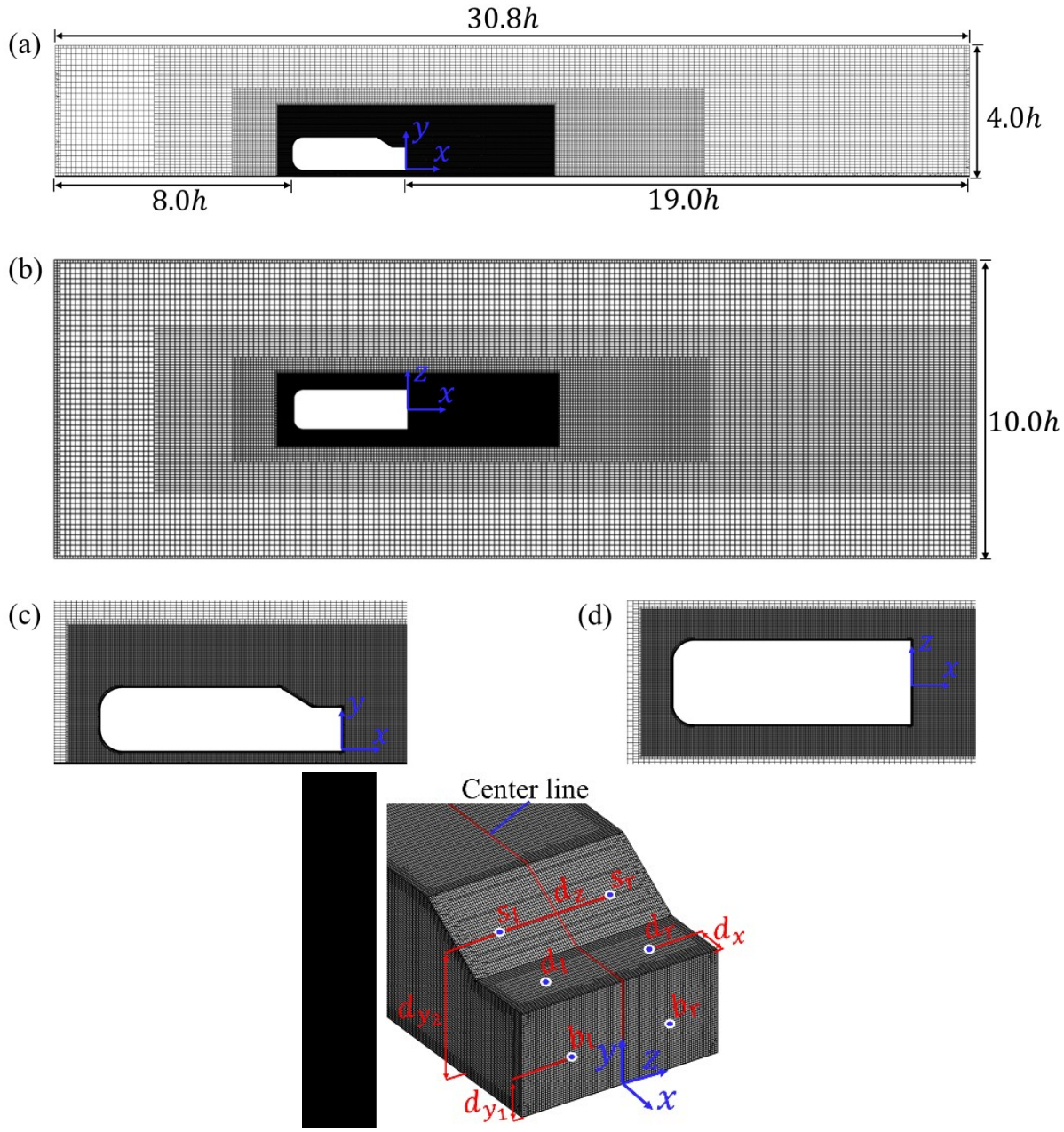

Figure 3.3: The computational domain. (a,c) side view of the mesh displayed on the symmetry plane ($z/h = 0$), (b,d) top view, and (e) surface mesh on the rear end of the Ahmed body. The blue dots on the rear end represent pressure coefficient monitoring points.

Following Kang et al., (2021), the mesh generated consists of hexahedral elements with four refinement levels as shown in Figure 3.3(a-d). The edges of the Ahmed body, identified as critical regions for inducing the asymmetric flow separation (He et al., 2021b), were also refined (Figure 3.3(e)). To characterize wake asymmetry, pressure coefficients (C_p) were obtained at both symmetric halves of the body at a spacing distance of $d_z = 0.834h$ in the z-direction. As shown in Figure 3.3(e), the C_p values were obtained on the mid-length of the slant (s_l, s_r), deck (d_l, d_r), and base of the trunk (b_l, b_r), and the corresponding gradients are denoted at $\partial C_{ps}/\partial z$, $\partial C_{pd}/\partial z$ and $\partial C_{pb}/\partial z$, respectively. The wall-normal distance of the data point on the slant and base is $d_{y_1} = 0.343h$, and $d_{y_2} = 0.844h$, respectively.

A detailed grid independence test was conducted using three different meshes (Coarse, Medium, and Fine) obtained by increasing the number of elements (Table 3.2). The test was performed using the SSA model based on initial model assessments. The results of y^+ on the ground (y_g^+) and the body (y_b^+), length of the reverse flow behind the trunk (L_r), C_D and C_L were used to evaluate the meshes. The value of L_r was determined at the streamwise distance between the base and the furthest extent of the isopleth of $U/U_\infty = 0$. Table 3.2 shows that for the medium and fine mesh, $y_g^+ < 1$ and $y_b^+ < 1$ indicating that the near wall mesh resolution was sufficient to resolve the viscous sublayer. Moreover, there are no significant difference in the values of L_r, C_D and C_L obtained from the medium and fine meshes. Therefore, to optimize computational cost, the medium mesh was used for all the simulations.

Table 3.2: Summary of properties for the grid independence test.

Mesh	Cell count	y_b^+	y_g^+	L_r/h	C_D	C_L
Coarse	7.9×10^6	1.19	1.62	0.762	0.347	0.145
Medium	20.8×10^6	0.62	0.54	0.769	0.346	0.150
Fine	40.9×10^6	0.12	0.10	0.769	0.346	0.150

3.3 Results and discussion

3.3.1 Turbulence model assessment and validation

Prior to performing the Reynolds number study, a RANS model assessment was performed to select the model that satisfactorily reproduces the results of previous experiments (He et al., 2022a) and LES (He et al., 2021b) using the notchback Ahmed body with $\beta_e = 17.8°$ and $Re = 5 \times 10^4$. Figure 3.4 shows the drag and lift coefficients predicted by the nine tested RANS turbulence models. The LES results of He et al., (2021b) using the same Reynolds number ($Re = 5 \times 10^4$) are included for comparison and validation. In terms of aerodynamic coefficients, the EB from the SMC models performed the best with less than 0.7% deviation for both drag and lift coefficients. Except for HRe SA, the results from the other models were within $\pm 5.8\%$ deviation compared with the LES results.

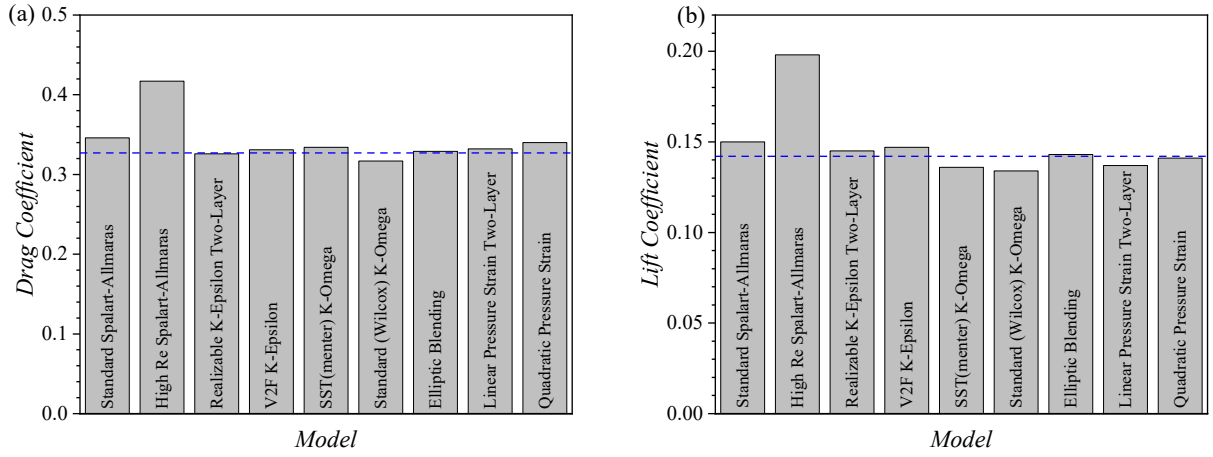

Figure 3.4: (a) Drag and (b) lift coefficients predicted from the RANS models at a Reynolds number, $Re = 5 \times 10^4$. The blue dash line represents the results of LES from He et al., (2021b) for a similar notchback Ahmed body and Reynolds number.

In addition to assessing the aerodynamic coefficients, it is important for the turbulence models to satisfactorily predict the asymmetric wake observed in the previous studies (He et al., 2021a, 2021b). Therefore, similar to He et al., (2021b), the streamwise mean velocity in the horizontal $(x - z)$ plane located at the mid-height of the slant (Figures 3.5(b)-3.5(d)) and the iso-surface of mean pressure coefficient, $C_p = -0.14$ (Figures 3.5(f)-3.5(h)) predicted by the RANS models are compared with the LES results (Figures 3.5(a) and 3.5(e)). The iso-surfaces are colored with the streamwise mean velocity, while the isopleth of $U/U_\infty = 0.3$ are shown on the contours to characterize the asymmetry. For brevity, the results for SSA, SST and EB models are shown in Figure 3.5. The results for HRe SA exhibited an asymmetric wake topology qualitatively similar to SSA, while the other EV and SMC models exhibited a symmetric wake that is qualitatively similar to the SST and EB models. The symmetric wake observed for SST agrees with previous model assessment study using SSTKO, LES, and Improved Delayed Detached Eddy Simulations (IDDES) by He et al., (2021b). The study showed that SSTKO was unable to predict the

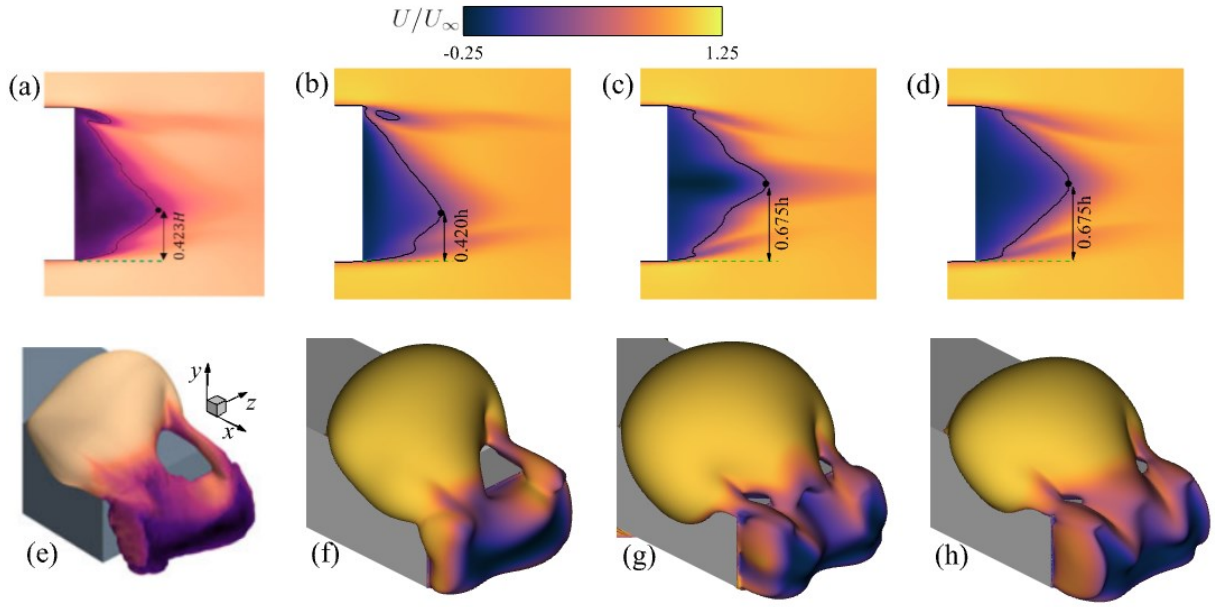

Figure 3.5: (a-d) Contours of streamwise mean velocity in the $(x - z)$ plane located at the mid-height of the slant and (e-h) iso-surfaces of pressure coefficient ($C_p = -0.14$) on the rear-end of the body for (a,e) LES, and (b-d,f-h) RANS.

asymmetric wake of the notchback Ahmed Body with $\beta_e = 17.8°$. Sims-Williams et al., (2011) also used the SSA model to simulate the wake flow of the notchback Ahmed body at $\beta_e = 17.8°$. While their unsteady RANS simulation successfully predicted asymmetry, their steady RANS simulation failed to do so. This disparity in results compared to the present steady RANS results, may be attributed to mesh resolution and refinement, particularly near the edges of the notchback model, which proved to be highly sensitive in inducing the asymmetric flow separation and associated wake topology. Between the SSA and HRe SA models, the spanwise distance from the side of the model to the farthest point on the $U/U_\infty = 0.3$ isopleth was $0.420h$ for SSA and $0.452h$ for HRe SA. Remarkably, the SSA results closely align with the LES results ($0.423h$) (He et al., 2021b). Additionally, as depicted in Figure 3.4, the aerodynamic coefficients predicted by SSA are comparable to those from LES. Consequently, the SSA model was chosen as the suitable model for the Reynolds number study.

3.3.2 Reynolds number effects on the wake characteristics

3.3.2.1 Pressure, aerodynamic and skin friction coefficients

The effects of Reynolds number on the iso-surfaces of mean pressure coefficient ($C_p = -0.14$) in the wake region of the body is presented in Figure 3.6. The iso-surfaces are colored by the streamwise mean velocity. For $Re = 5 \times 10^3$ and $Re = 1 \times 10^4$, the iso-surfaces exhibit symmetry over the slant, deck, and at the base of the truck. However, the toroidal structure at the base of $Re = 5 \times 10^3$ is partially formed compared to $Re = 1 \times 10^4$. As Reynolds number increases, $Re > 1 \times 10^4$, the wake structure gradually transitions to an asymmetric topology. Although $Re = 2 \times 10^4$ and $Re = 4 \times 10^4$ exhibit a left-skewed asymmetry, while $Re = 3 \times 10^4$ and $Re = 5 \times 10^4$ show a right-skewed asymmetry, the directional preference is stochastic and

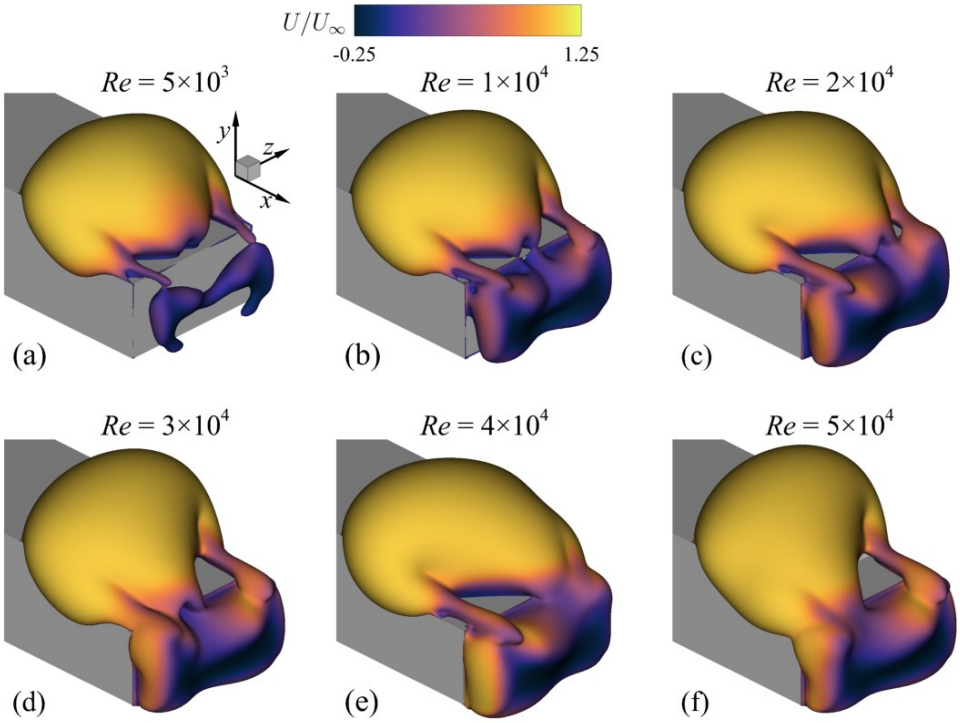

Figure 3.6: Iso-surfaces of mean pressure coefficient ($C_p = -0.14$) for (a) $Re = 5 \times 10^3$, (b) $Re = 1 \times 10^4$, (c) $Re = 2 \times 10^4$, (d) $Re = 3 \times 10^4$, (e) $Re = 4 \times 10^4$ and (f) $Re = 5 \times 10^4$. The iso-surfaces are colored by the streamwise mean velocity.

depends on the first onset of instability in the laminar regime (Evstafyeva et al., 2017; Grandemange et al., 2012). Moreover, the steady RANS is unable to demonstrate evidence of bimodality, but its occurrence is anticipated based on insights from previous studies on 3D bluff bodies (Grandemange et al., 2014; He et al., 2021b; Kang et al., 2021).

To characterize the wake asymmetry on the slant, deck and base of the body, the distribution of the gradients of the pressure coefficients ($\partial C_{ps}/\partial z$, $\partial C_{pd}/\partial z$ and $\partial C_{pb}/\partial z$) from the specified locations in Figure 3.3(b) is presented in Figure 3.7(a). At $Re = 5 \times 10^4$, the value of $\partial C_{pd}/\partial z = 0.628$ agrees with the values of $\partial C_{pd}/\partial z = 0.625$ (experiments) and 0.649 (LES) reported in He et al., (2021b), further validating the present simulations based on the SSA model. For $Re \leq 1 \times 10^4$, all the gradients are zero, in agreement with the symmetry wake topology. However, as Reynolds number increases, the gradient on the slant and the deck increases rapidly,

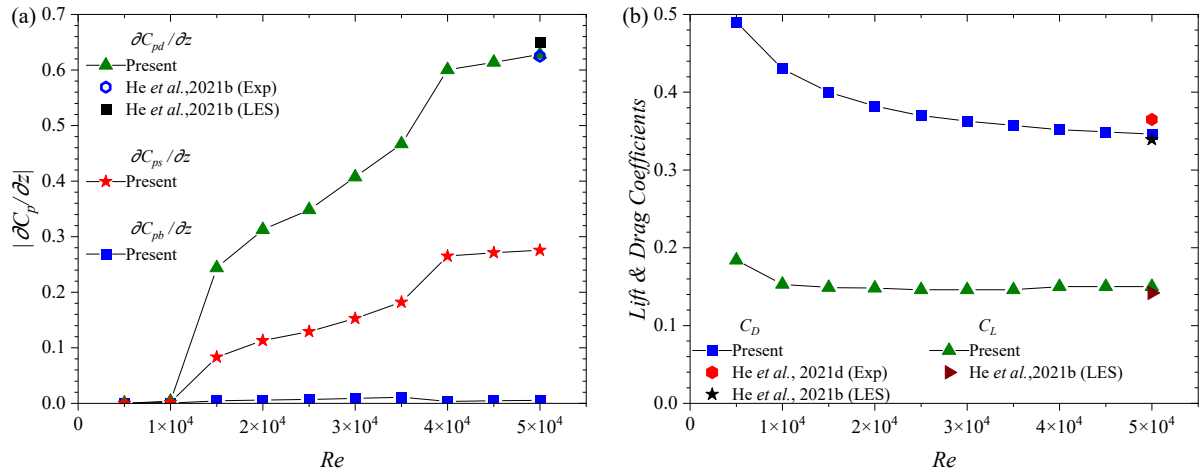

Figure 3.7: Distribution of (a) absolute value of the mean gradient of the pressure coefficient ($|\partial C_p/\partial z|$), and (b) lift ($C_L$) and drag ($C_D$) coefficients. The drag coefficient, the lift coefficient, and the mean gradient of the pressure coefficient on the deck at $Re = 5 \times 10^4$ are compared to results of experiment and LES from He et al., 2021b and He et al., 2021d.

especially on the deck. In contrast, the gradient on the base is negligible and independent of Reynolds numbers. This observation implies that the asymmetry is more pronounced on the deck, while the wake structure behind the base remains symmetric. The present observation is consistent with the findings of He et al., (2021b) for $Re = 5 \times 10^4$. The effects of the Reynolds number on the lift and drag coefficients are shown in Figure 3.7(b). The drag coefficient decreases with increasing the Reynolds number and remains nearly constant ($C_D \approx 0.352$) for $Re \geq 3.5 \times 10^4$. In contrast, the lift coefficient plateaus at $C_L \approx 0.146$ for $Re_h \geq 1 \times 10^4$. These asymptotic values are consistent with the results reported in He et al., (2021b) at $Re = 5 \times 10^4$.

Contours of the skin friction coefficient ($C_f = 2\tau_w/(\rho U_\infty^2)$) on the rear-end of the body for selected test case, ($Re = 5 \times 10^3$, 2×10^4 and 5×10^4) are shown in Figure 3.8, where τ_w is the wall shear stress. For $Re = 5 \times 10^3$ and 1×10^4, the contours of the C_f show a symmetric distribution with enhanced C_f along the edges and in regions where the separated flow attaches onto the deck (see Figure 3.10). As Reynolds number increases, $Re \geq 1 \times 10^4$, the C_f along the edges of the slant exhibits asymmetry, signifying asymmetric separation from both the

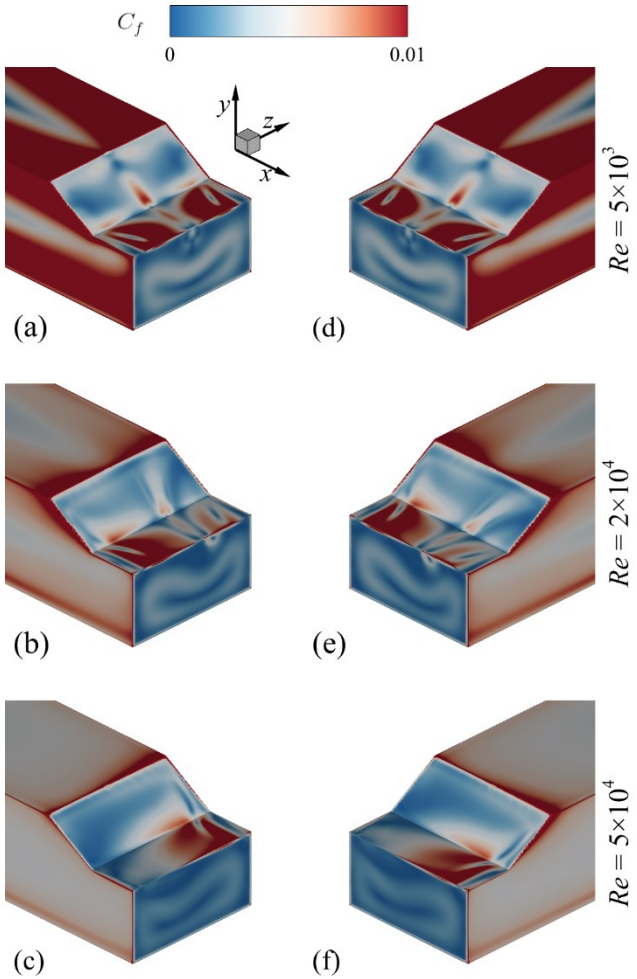

Figure 3.8: Contours of skin friction coefficient (C_f) for (a,d) $Re = 5 \times 10^3$, (b,e) $Re = 2 \times 10^4$, and (c,f) $Re = 5 \times 10^4$. Left side (a-c) and right side (d-f).

roof and C-pillars of the notchback. The asymmetric separation from the roof is also consistent with observations in He et al., (2021a). On the deck, the C_f also demonstrates asymmetric reattachment in agreement with He et al., (2021a). Profiles of the skin friction coefficient along $z/h = -0.417$, 0.0, and 0.417 and the slant and deck are shown in Figure 3.9. It should be noted that for the asymmetric cases, $Re \geq 1 \times 10^4$, the profiles of C_f at $z/h = \pm 0.417$ were matched based on the signs of C_p on the deck locations, d_l and d_r (Figure 3.3(b)), to facilitate comparison. Here, the side of the deck where the wake is skewed towards has negative C_p, while the opposite

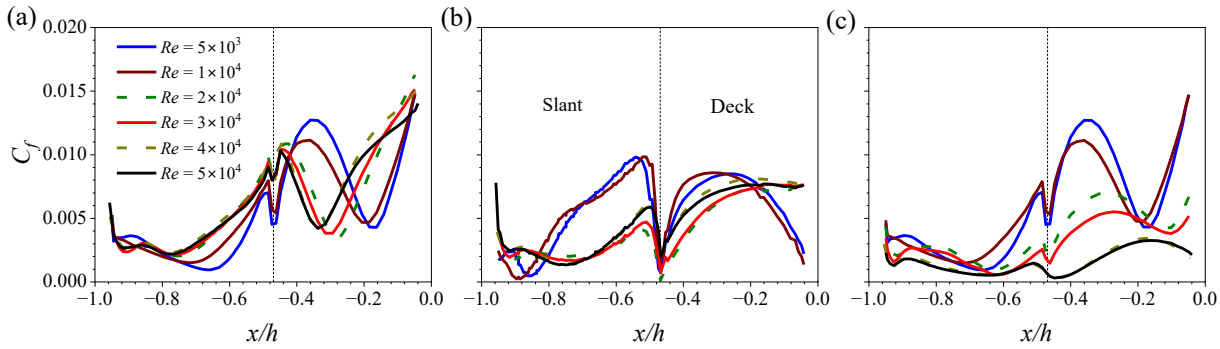

Figure 3.9: Profiles of the C_f on the slant and the deck. The profiles are extracted on the surface of the body at (a) $z/h = -0.417$, (b) $z/h = 0$, and (c) $z/h = 0.417$.

side has positive C_p (see Figure 3.6). The profiles demonstrate that the degree of asymmetry increases with Reynolds number and converges for $Re > 3 \times 10^4$.

3.3.2.2 Reverse flow region

To further investigate the effects of the Reynolds number on the wake characteristics, Figure 3.10 shows the iso-surfaces of streamwise mean velocity ($U/U_\infty = 0$) to visualize the reverse flow regions ($U < 0$) around the body. The iso-surfaces are colored with pressure coefficients. The reverse flow region near fore-end of the body reduces with increasing Reynolds number. The reverse flow also exhibits asymmetry on the slant and the deck, which becomes stronger as Reynolds number increases. For each test case, the separated flow from the roof and sides of the slant attaches to the deck. However, the farthest attachment point, located near the trailing edge of the deck, demonstrates a fully separated flow that spills over the deck and alters the shape of the reverse flow region behind the base. This highlights the highly three-dimensional nature of the reverse flow region on the rear-end of the notchback Ahmed body.

Accordingly, the volume of the reverse flow region is determined to characterize the separated flow on the slant, deck and behind the base of the body. Analogous to reverse flow area formulation proposed by Pearson et al., (2013), the reverse flow volume is calculated as follows:

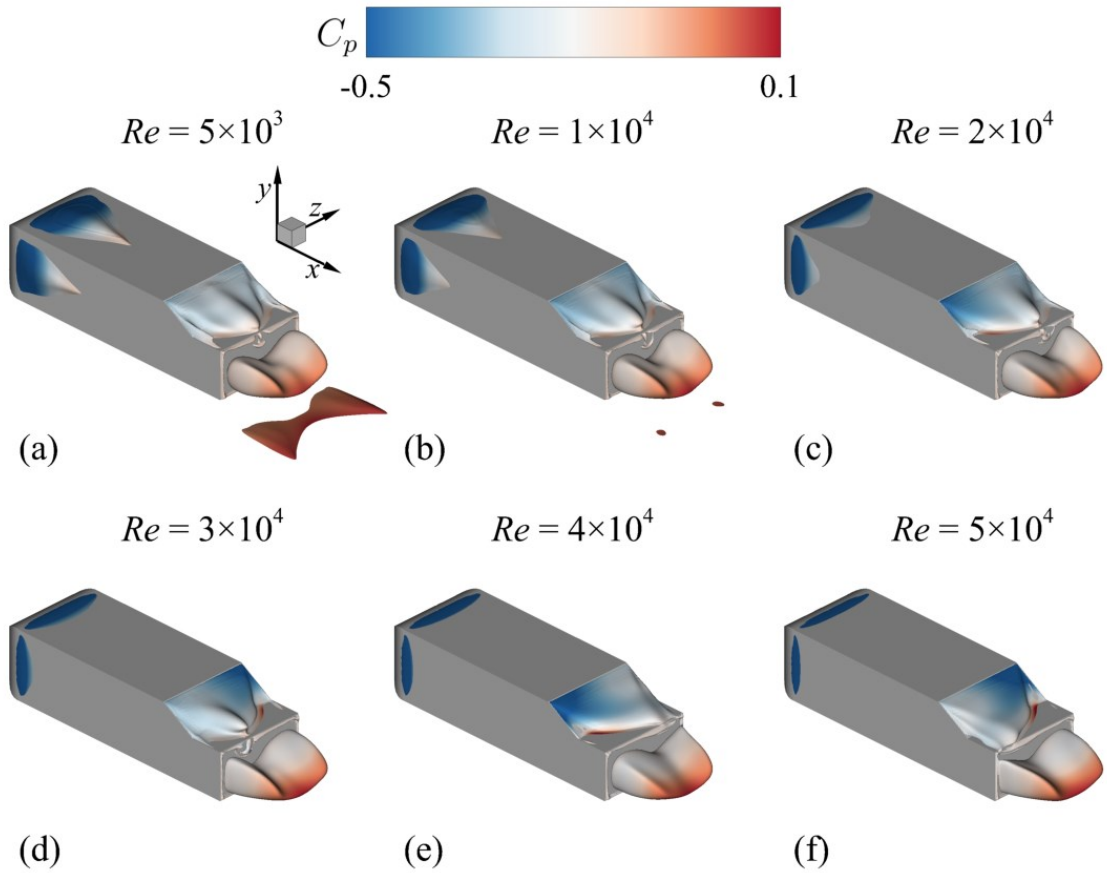

Figure 3.10: Iso-surfaces of reverse flow region ($U/U_\infty = 0$) for (a) $Re = 5\times10^3$, (b) $Re = 1\times10^4$, (c) $Re = 2\times10^4$, (d) $Re = 3\times10^4$, (e) $Re = 4\times10^4$ and (f) $Re = 5\times10^4$. The iso-surfaces are colored by the pressure coefficient.

$$V_i = \int_M \mathcal{H}\big(U(x,y,z)\big)dx\,dy\,dz \tag{3.10}$$

$$\mathcal{H}(p) = \begin{cases} 0 & p \geq 0 \\ 1 & p < 0 \end{cases} \tag{3.11}$$

where U is the streamwise mean velocity, $\mathcal{H}(p)$ is the detector function based on the event $p = U(x,y,z)$ for each grid size and dx, dy, and dz are the vector spacing in the x, y and z directions, respectively. For the reverse flow volume on the slant and deck, V_{s-d}, the masked region M was defined as $x/h \in [-1.0,0.0]$, $y/h \in [0.7,1.0]$ and $z/h \in [-0.7,0.7]$ while for the base region, V_b , $x/h \in [0.0,1.1]$, $y/h \in [0.0,0.7]$ and $z/h \in [-0.7,0.7]$. It should be noted that the Ahmed body

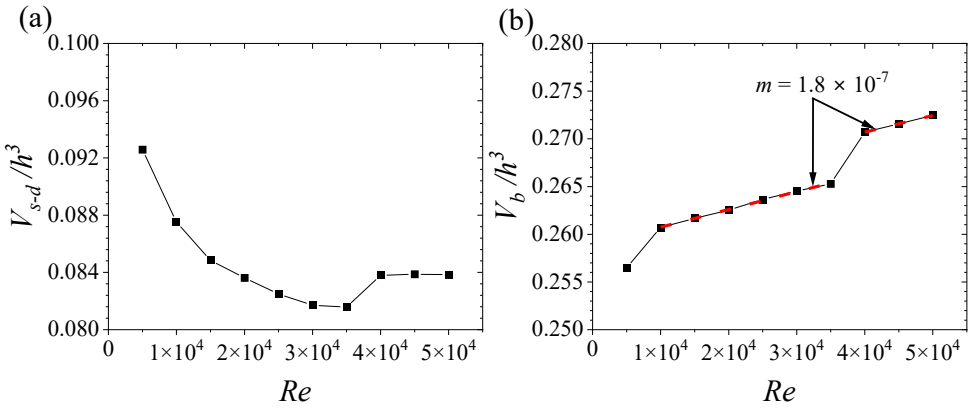

Figure 3.11: Distribution of the mean reverse flow volume (a) over the slant-deck region and (b) behind the base of the body.

was blanked out in the velocity field before computing the volumes. Figure 3.11 shows the distribution of the normalized reverse flow volumes, V_{s-d} and V_b. On the slant and deck (Figure 3.11(a)), the reverse flow volume decreases with increasing Reynolds number for $Re \in [5 \times 10^3, 3.5 \times 10^4]$ and then increase marginally and stays constant, ($V_{s-d}/h^3 = 0.084$), for $Re \in [4 \times 10^4, 5 \times 10^4]$. Behind the base of the body, the distribution of V_b/h^3 demonstrates a stepwise increase with Reynolds number, with a slope of $m = 1.8 \times 10^{-7}$ in the regimes, $Re \in [1 \times 10^4, 3.5 \times 10^4]$ and $Re \in [4 \times 10^4, 5 \times 10^4]$.

In §3.3.2.1, gradients of the pressure coefficients showed that the asymmetry is more pronounced on the deck than the slant. Therefore, the wetted reverse flow area (A) on the deck and spanwise barycenter (z_g) are used to provide further insight into effects of Reynolds number on the wake asymmetry. The wetted reverse flow area is represented by the isopleth of $U = 0$ on a spanwise plane located one grid point above the surface deck. The area (A) was computed using a similar formulation as the reverse flow volume, but in a plane ($x - z$). The spanwise barycenter is determined as:

$$z_g = \frac{\int_M z\,\mathcal{H}\big(U(x,z)\big)dx\,dz}{\int_M \mathcal{H}\big(U(x,z)\big)dx\,dz} \tag{3.12}$$

$$\mathcal{H}(p) = \begin{cases} 0 & p \geq 0 \\ 1 & p < 0 \end{cases} \tag{3.13}$$

where z is the spanwise position of the grid of size, dx and dz. Here, the masked region is defined as $x/h \in [-0.5,0.0]$ and $z/h \in [-0.7,0.7]$ for both A and z_g. Figure 12 shows the contours of wetted reverse flow area and the distributions of the normalized A and the magnitude of the spanwise barycenter $|z_g|$. For $Re \leq 1 \times 10^4$, the contours of wetted reverse flow area exhibit a symmetric topology, as confirmed by Figure 3.12(b), which shows a zero barycenter (i.e., located on the centerline). As the Reynolds number increases, both the contours and the barycenter distribution demonstrate asymmetry. The wetted reverse flow area (Figure 3.12(c)) also shows a distribution consistent with V_{s-d} (Figure 3.11(a)). Based on the presented results, especially in Figure 3.7(a), Figure 3.10 - Figure 3.12, the time-averaged wake structure of the notchback Ahmed body is categorized into three Reynolds number regimes: symmetric ($Re \leq 1 \times 10^4$), transitionally asymmetric ($1 \times 10^4 < Re \leq 3.5 \times 10^4$), and fully asymmetric ($Re > 3.5 \times 10^4$).

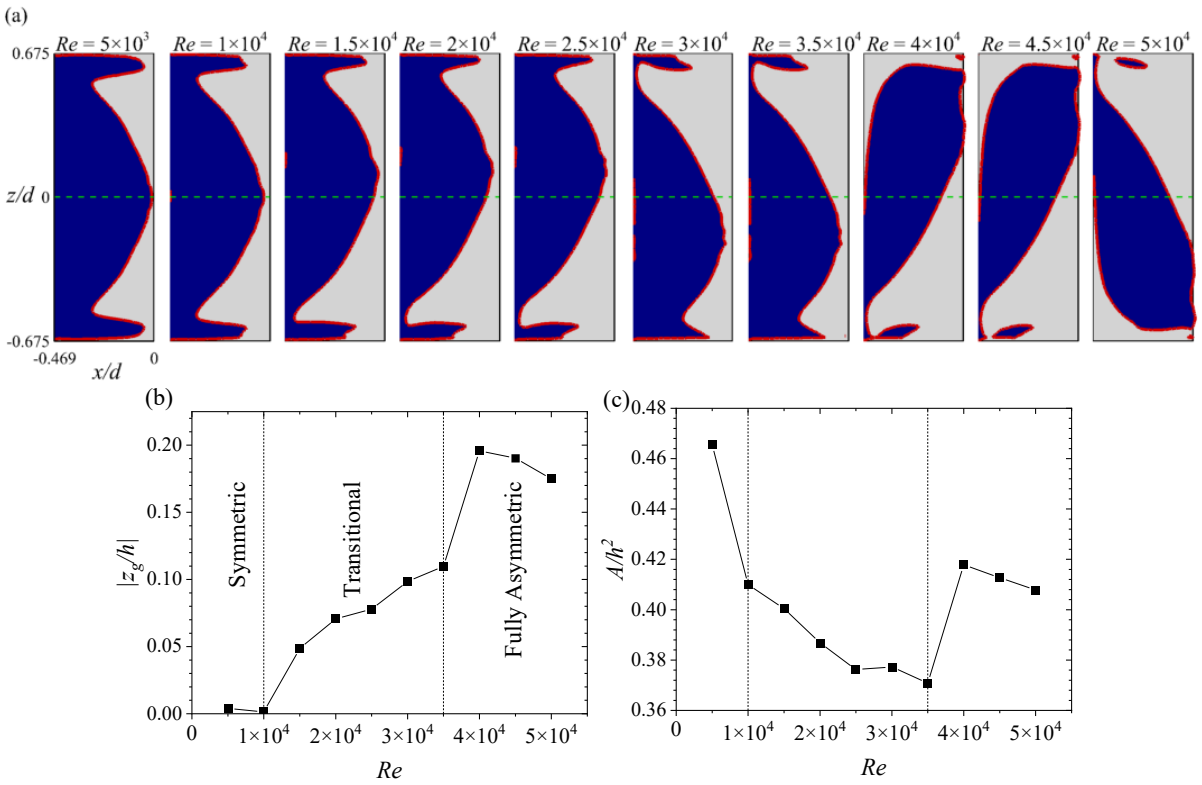

Figure 3.12: (a) Contours of the wetted reverse flow area on the deck and the distribution of (b) absolute value of the spanwise barycenter and (c) mean reverse flow area on the deck.

3.3.2.3 Mean velocities, vorticities, and Q-criterion.

Figure 3.13 shows contours of the wall-normal mean velocity (V) for $Re = 5 \times 10^3$, 2×10^4 and 5×10^4 obtained at three spanwise locations: symmetry ($z/h = 0.0$) and off-symmetry ($z/h = \pm 0.417$). In each plot, the zero-contour line $U/U_\infty = 0$ is used to demarcate the reverse flow regions and the mean streamline are superimposed to reveal the flow pattern. The wake region of the notchback Ahmed body is characterized by three recirculation bubbles: one on the slant and two vertically arranged behind the back. For $Re = 5 \times 10^3$, the two offset planes depict the symmetric topology with attached flow on the deck. The symmetry plane ($z/h = 0$) demonstrates a fully separated flow over the deck, consistent with Figure 3.10. The contours also indicate that downwash flow ($V < 0$) is stronger in the symmetry plane, whereas upwash flow

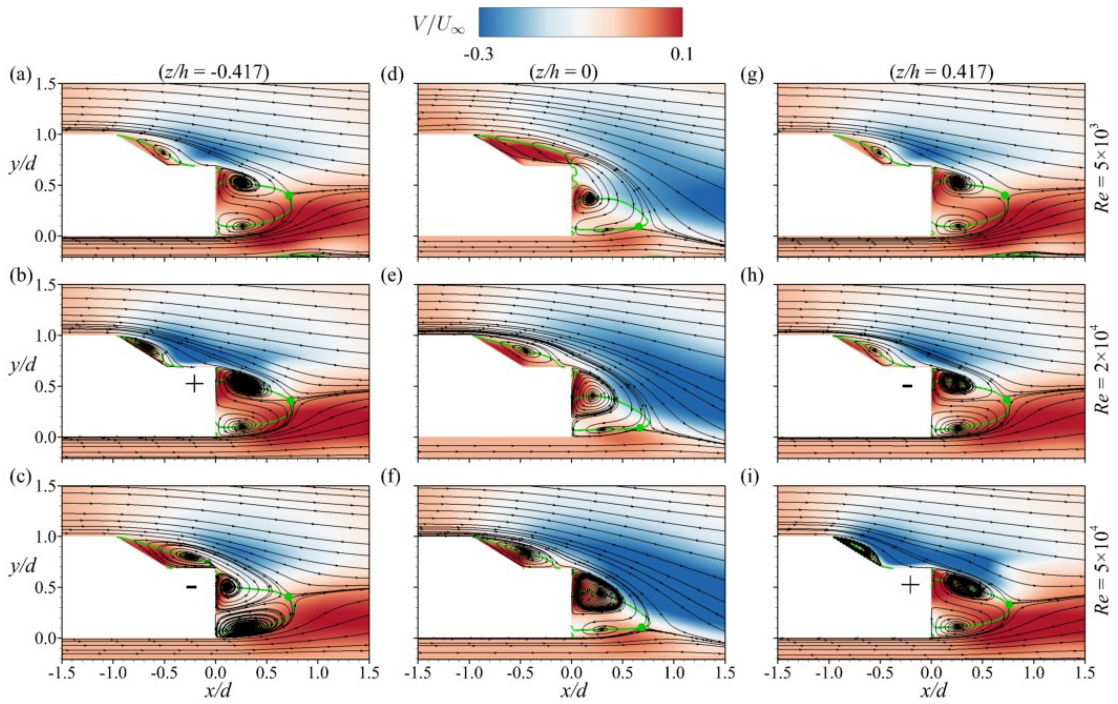

Figure 3.13: Contours of wall-normal mean velocity for (a,c,g) $Re = 5 \times 10^3$, (b,e,h) $Re = 2 \times 10^4$ and (c,f,i) $Re = 5 \times 10^4$. Superimposed on the contours are the mean streamlines. The green line represents the isopleth of $U/U_\infty = 0$ which bounds the reverse flow region and the green dot is the saddle point. The (+) and (-) represent the signs of C_p on the deck.

($V > 0$) is dominant in the off-symmetry planes. Consequently, the saddle point of the recirculation bubbles behind the base is closer to the wall in the symmetry plane, whereas the saddle points in the off-symmetry planes are away from the wall. For the asymmetric cases (e.g., $Re = 2 \times 10^4$ and $Re = 5 \times 10^4$), the downwash is more intense in the symmetry plane compared to the symmetric cases (e.g., $Re = 5 \times 10^3$). Moreover, the positive C_p side (Figures 3.13(b) and 3.13(i)) is associated with stronger downwash, which induces earlier reattachment of the flow separated from the roof onto the deck compared to the negative C_p side (Figures 3.13(c) and 3.13(h)). As Reynolds number increases, this effect intensifies leading to a fully separated flow on the negative C_p side (Figure 3.13(c)).

The entrainment of fluid from the sides of the slant and the base of the body is examined using the contours of the spanwise mean velocity obtained at the mid-height of the slant (Figures 3.14(a)

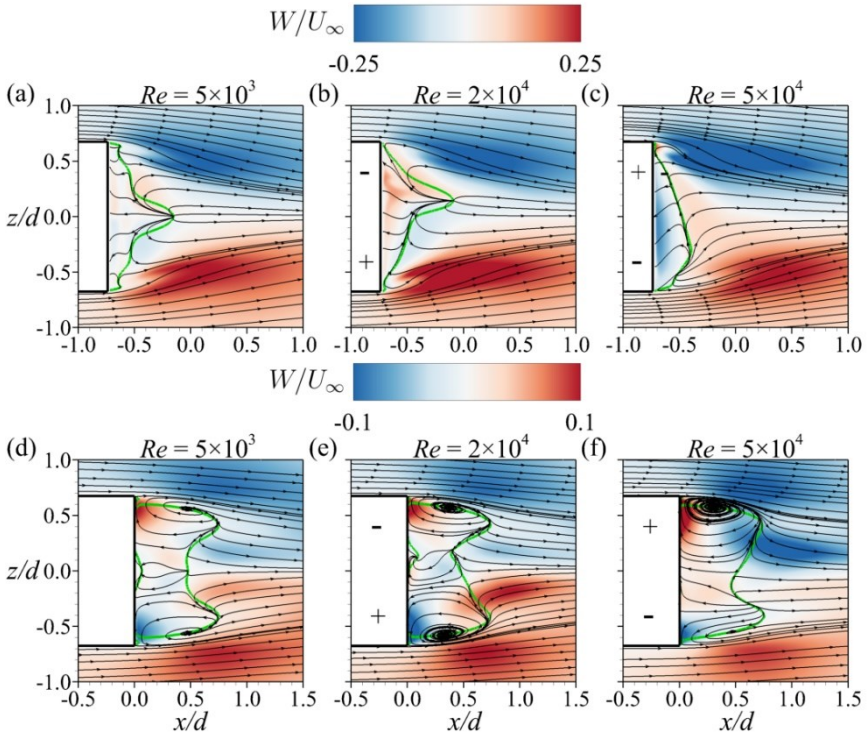

Figure 3.14: Contours of spanwise mean velocity for (a,d) $Re = 5 \times 10^3$, (b,e) $Re = 2 \times 10^4$ and (c,f) $Re = 5 \times 10^4$. Superimposed on the contours are the mean streamlines. The green line represents the isopleth of $U/U_\infty = 0$ which bounds the reverse flow region. The contours are extracted in the $(x - z)$ planes located at (a-c) $y/h = 0.343$, and (d-f) $y/h = 0.844$. The (+) and (-) represent the signs of C_p on the deck.

– 3.14(c)) and the base (Figures 3.14(d) – 3.14(f)). The plots for the asymmetric cases show that entrainment from the sides of both the slant and base is more intense on the attached flow side (i.e., positive C_p) of the body, while the symmetric cases demonstrate an equal balance in entrainment from the sides of the body.

Figure 3.15 shows the contours of the streamwise mean vorticity in the cross-plane with the streamlines superimposed, and the vortical structures visualized with the iso-surface of the Q-criterion (He et al., 2021a). A threshold of $Q(h/U\infty)^2 = 0.45$ was used to depict the salient structures at the rear-end of the body, including the C-pillar vortices emanating from the side edges of the slant. For $Re = 5 \times 10^3$, the streamlines demonstrate symmetric entrainment from the sides of the body, resulting in symmetric streamwise mean vorticity (Figure 3.15(a)) distribution

and vortical structures (Figure 3.15(d)). On the other hand, uneven entrainment and asymmetric vortical structures are observed as Reynolds number increases.

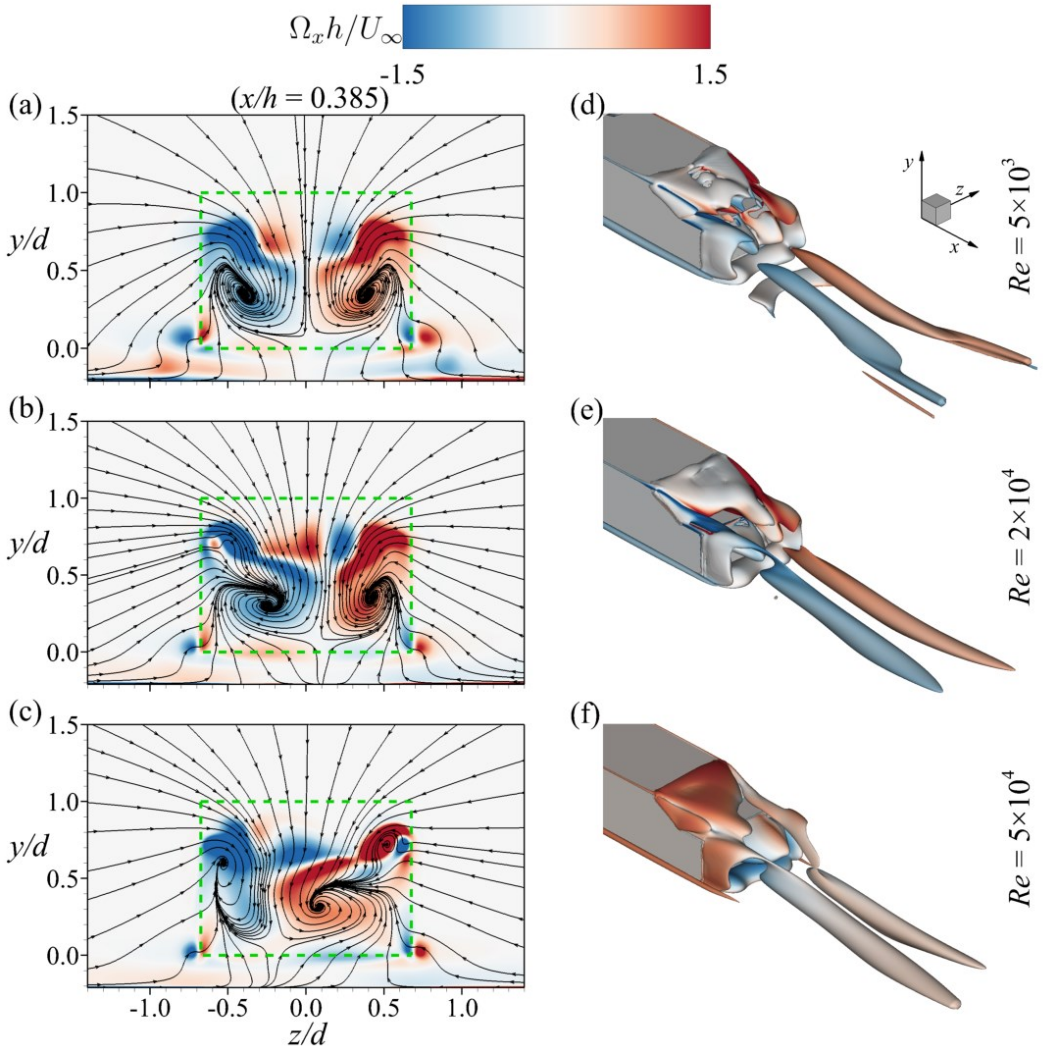

Figure 3.15: (a-c) Contours of streamwise mean vorticity and (d-f) iso-surface of Q-criterion ($Q(h/U_\infty)^2 = 0.45$) for (a,d) $Re = 5 \times 10^3$, (b,e) $Re = 2 \times 10^4$, and (c,f) $Re = 5 \times 10^4$. The contours of the streamwise mean vorticity are shown in the $(y - z)$ plane located at $x/h = 0.385$. The mean streamlines are superimposed on the contours. The iso-surfaces of the Q-criterion are colored by the streamwise mean vorticity.

The source of the asymmetry in the vorticity field can be examined using the tilting and stretching terms in the vorticity transport equation (Crane et al., 2022). For a steady, viscous, incompressible fluid, the mean vorticity transport equation is given as

$$U_j \frac{\partial \Omega_i}{\partial x_j} = \underbrace{\Omega_j \frac{\partial U_i}{\partial x_j}}_{(I)} + \underbrace{\overline{\omega_j' \frac{\partial u_i'}{\partial x_j}}}_{(II)} + \frac{\partial}{\partial x_j}\left(\underbrace{\nu \frac{\partial \Omega_i}{\partial x_j}}_{(III)} - \underbrace{\overline{u_j' \omega_i'}}_{(IV)} \right) \tag{3.14}$$

where Ω_i and ω_i' are the mean and fluctuating vorticity components, respectively, term (I) is the mean stretching/tilting of vorticity by the mean flow, term (II) is the fluctuating stretching/titling term, and terms (III) and (IV) represent the viscous and turbulent diffusion terms, respectively. The term (I) can be divided into mean stretching (S_i) and tilting (T_i) components. For example, the stretching and tilting terms that contribute to the generation of streamwise mean vorticity are given as:

$$\Gamma_x = \Omega_j \frac{\partial U}{\partial x_j} = \underbrace{\Omega_x \frac{\partial U}{\partial x}}_{S_x} + \underbrace{\Omega_y \frac{\partial U}{\partial y} + \Omega_z \frac{\partial U}{\partial z}}_{T_x} \tag{3.15}$$

Figure 3.16 shows iso-surfaces of the mean stretching/tilting terms, Γ_x, Γ_y and Γ_z, for the streamwise, wall-normal and spanwise components of mean vorticity, respectively. The results are presented for both a symmetric case ($Re = 5 \times 10^3$) and an asymmetric case ($Re = 5 \times 10^4$) to facilitate comparison. In each test case, the magnitude of the term Γ_z was consistently the largest, followed by Γ_y and Γ_x. The term, Γ_x is primarily linked to shear layers generated from the corners and edges of the body, while Γ_y is predominantly associated with the sides and C-pillars. The term, Γ_z is mainly linked to the separated shear layers from the leading and rear spanwise edges of the body. For $Re = 5 \times 10^3$, the topology of the mean stretching/tilting terms are symmetric.

However, for $Re = 5 \times 10^4$, Γ_x (Figures 3.16(d)- 3.16(f)) exhibits pronounced asymmetry on the roof towards the trailing edge, slant, and deck. For example, Γ_x contributes to the formation of a strong C-pillar vortex and shear layer over on the right-side of the slant (Figure 3.16(d)). The plots of Γ_y and Γ_z (Figures 3.16(e) and 3.16(f)) also demonstrate asymmetric shear layers over the slant and deck of the body. These results support the earlier notion that the wake's asymmetry is primarily induced by the uneven flow over the roof, leading to separation over the trailing edge and asymmetric entrainment from the sides of the slant of the notchback Ahmed body.

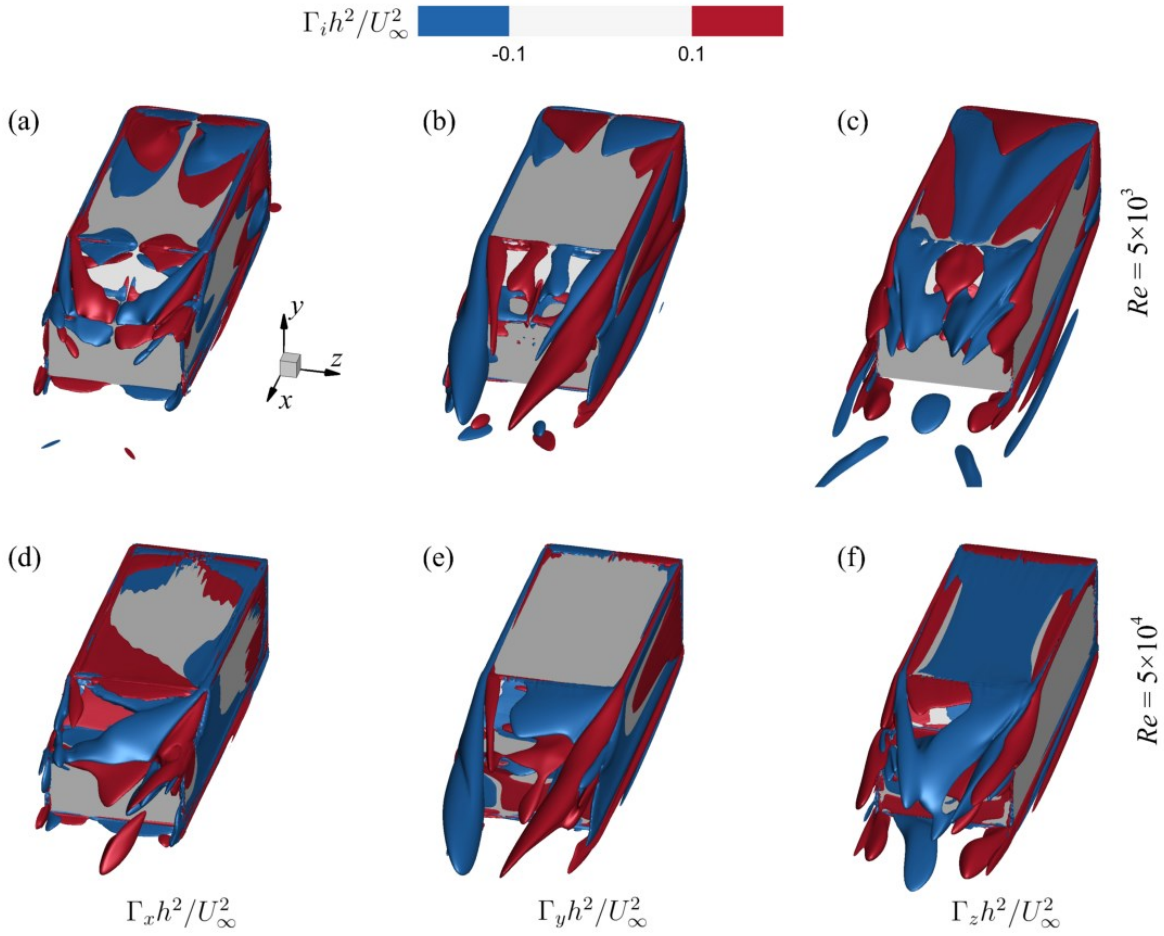

Figure 3.16: Iso-surface of (a,d) streamwise, (b,e) wall-normal and (c-f) spanwise tilting/stretching terms ($\Gamma_i h^2/U_\infty^2 = \pm 0.1$) of the vorticity transport equation for (a-c) $Re = 5 \times 10^3$, (b,e) and (d-f) $Re = 5 \times 10^4$.

To further examine the individual roles of the stretching and tilting terms in the generation of the mean vorticity field and the wake asymmetry, iso-surfaces of S_i and T_i for $Re = 5 \times 10^4$ are presented in Figure 3.17. On the roof of the body, $T_x = \Omega_y(\partial U/\partial y) + \Omega_z(\partial U/\partial z)$ is the major source of the asymmetry observed in Γ_x for Ω_x, while $S_x = \Omega_x(\partial U/\partial x)$ acts as sink. Behind the body, the asymmetry in Ω_x and the associated C-pillar vortices are generated by both T_x and S_x, with S_x as the dominant source. In Figures 3.17(d) – 3.17(f), the stretching term, $S_y = \Omega_y(\partial V/\partial y)$ contributes to the asymmetry of the C-pillars, while the tilting term, $T_y = \Omega_x(\partial V/\partial x) + \Omega_z(\partial V/\partial z)$ is the major source of the asymmetric distribution of Ω_y from the trailing-edge of the roof and over the slant. Due to the dominance of T_y, the iso-surface of Γ_y mimics T_y. For Ω_z, the stretching term, $S_z = \Omega_z(\partial W/\partial z)$ (Figure 3.17(h)) is the primary source, while $T_z = \Omega_x(\partial W/\partial x) + \Omega_y(\partial W/\partial y)$ (Figure 3.17(g)) enhances Ω_z, particularly along the C-pillars.

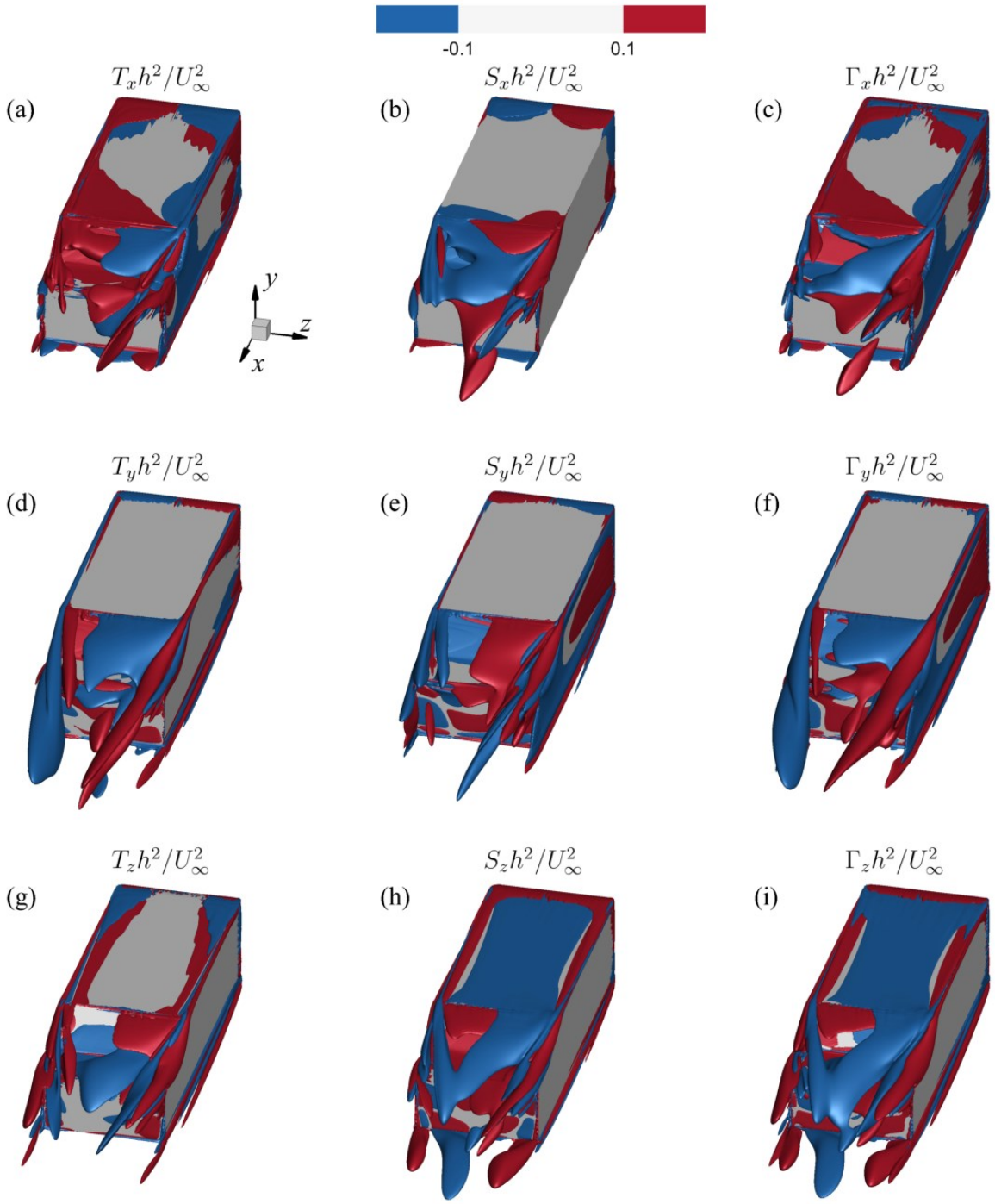

Figure 3.17: Iso-surface of (a-c) streamwise, (d-f) wall-normal and (g-i) spanwise tilting (a,d,g), stretching (b,e,h), and tilting/stretching (c,f,i) terms for $Re = 5 \times 10^4$.

Chapter 4

Conclusion

4.1 Summary and conclusion

This thesis investigated the effects of Reynolds number on the wake characteristics of a notchback Ahmed body with effective backlight angle $\beta_e = 17.8°$ reported by previous studies to produce an asymmetric wake. Prior to the main investigation, a RANS turbulence model assessment was performed to select the model that satisfactorily reproduces the time-averaged results from previous investigations using experiments and large eddy simulations. A total of nine turbulence models including both eddy viscosity and second moment closure models were tested. The eddy viscosity models consist of two one-equation models (i.e, standard Spalart-Allmaras and high Re Spalart-Allmaras), and four two-equation models divided into two epsilon-based (realizable k-epsilon two layers, V2F k-epsilon) and two omega-based (standard k-omega and SST k-omega) models. Among all the tested models, only the standard Spalart-Allmaras model was able to accurately predict both the aerodynamic coefficients and the time-averaged wake asymmetry of the notchback Ahmed body with $\beta_e = 17.8°$ and at Reynolds number, $Re = 5 \times 10^4$. Therefore, the standard Spalart-Allmaras model was selected for the Reynolds number study.

The Reynolds number investigation was performed using ten Reynolds numbers spanning a wide range of low ($Re = 5 \times 10^3$) to high Reynolds numbers ($Re = 5 \times 10^4$) at an interval of 5000. The results showed that the drag coefficient decreased with increasing Reynolds number while the lift coefficient plateaus at $C_L = 0.146$ for $Re \geq 1 \times 10^4$. The iso-surfaces of mean

pressure coefficient, the gradients of the pressure coefficient on the slant, deck and base, and the statistics of the reverse flow region were used to characterize the wake topology. Three main wake regimes were identified based on the Reynolds number. For $Re \leq 1 \times 10^4$, the wake characteristics exhibited symmetry about the centerline of the body. The reverse flow volume over the slant decreased as Reynolds number increased from $Re = 5 \times 10^3$ to 1×10^4, whereas the reverse flow volume behind the base increased with increasing Reynolds number. Within the transitional regime, $1 \times 10^4 < Re \leq 3.5 \times 10^4$, the wake transitions from a symmetric to a fully asymmetric regime at $Re > 3.5 \times 10^4$.

Contours of skin friction coefficient on the body surface, and iso-surface of Q-criterion revealed an asymmetric separation of the flow from both the roof and the C-pillars for the transitional and fully asymmetric regimes. Wall-normal and spanwise mean velocity in vertical and horizontal planes also demonstrated a strong imbalance in entrainment from the sides of the body. The asymmetry of the flow for $Re > 1 \times 10^4$ was attributed to both asymmetric separation and imbalance in entrainment and was further investigated using the mean stretching/tilting terms of the vorticity transport equation. The roof asymmetry was found to be generated by the tilting of streamwise mean vorticity, while the C-pillar asymmetry results from the stretching of streamwise and wall-normal vorticities, as well as the tilting of spanwise vorticity.

4.2 Recommended future work

The present study used RANS to investigate the flow around a notchback Ahmed body. Although the Spalart-Allmaras model was able to reproduce time-averaged results of large eddy simulation, important flow feature such as bi-modality and the vortex shedding cannot be

investigated. Further investigations using scale resolving simulations or time-resolved experiment will provide useful insight into the unsteadiness of the flow field around the notchback Ahmed body. Special attention could be given to the Reynolds number range of $Re \in [1 \times 10^4, 1.5 \times 10^4]$ and $Re \in [3.5 \times 10^4, 4 \times 10^4]$ to gain better insight into the transition of the unsteady 3D wake structure from symmetric to fully asymmetric states.

References

Ahmed, S. R., Ramm, G., & Faltin, G. (1984). Some salient features of the time -averaged around vehicle wake. *SAE Transactions*, *93*, 473–503. https://about.jstor.org/terms

Bonnavion, G., & Cadot, O. (2018). Unstable wake dynamics of rectangular flat-backed bluff bodies with inclination and ground proximity. *Journal of Fluid Mechanics*, *854*, 196–232. https://doi.org/10.1017/jfm.2018.630

Bruneau, C. H., Creusé, E., Depeyras, D., Gilliéron, P., & Mortazavi, I. (2010). Coupling active and passive techniques to control the flow past the square back Ahmed body. *Computers and Fluids*, *39*(10), 1875–1892. https://doi.org/10.1016/j.compfluid.2010.06.019

Bruneau, C.-H., Creusé, E., Depeyras, D., Gilliéron, P., & Mortazavi, I. (2011). Active procedures to control the flow past the Ahmed body with a 25° rear window. *International Journal of Aerodynamics*, *1*, 299–317. https://doi.org/10.1504/IJAD.2011.038847

Cogotti, A. (1986). Car-wake imaging using a seven-hole probe. *SAE Transactions*, 1071–1095. https://about.jstor.org/terms

Crane, R. J., Popinhak, A. R., Martinuzzi, R. J., & Morton, C. (2022). Tomographic PIV investigation of vortex shedding topology for a cantilevered circular cylinder. *Journal of Fluid Mechanics*, *931*, R1. https://doi.org/10.1017/jfm.2021.904

Dalla Longa, L., Evstafyeva, O., & Morgans, A. S. (2019). Simulations of the bi-modal wake past three-dimensional blunt bluff bodies. *Journal of Fluid Mechanics*, *866*, 791–809. https://doi.org/10.1017/jfm.2019.92

Davidson, L., Nielsen, P., & Sveningsson, A. (2003). Modification of the v2f model for computing the flow in a 3D wall jet. *Turbulence, Heat and Mass Transfer*, *4*, 577–584.

Durbin, P. A. (1996). On the k-3 stagnation point anomaly. *International Journal of Heat and Fluid Flow*, *17*(1), 89–90.

Evstafyeva, O., Morgans, A. S., & Dalla Longa, L. (2017). Simulation and feedback control of the Ahmed body flow exhibiting symmetry breaking behaviour. *Journal of Fluid Mechanics*, *817*, R2. https://doi.org/10.1017/jfm.2017.118

Fan, Y., Xia, C., Chu, S., Yang, Z., & Cadot, O. (2020). Experimental and numerical analysis of the bi-stable turbulent wake of a rectangular flat-backed bluff body. *Physics of Fluids*, *32*(10), 105111. https://doi.org/10.1063/5.0019794

Gibson, M. M., & Launder, B. E. (1978). Ground effects on pressure fluctuations in the atmospheric boundary layer. *Journal of Fluid Mechanics*, *86*(3), 491–511. https://doi.org/10.1017/S0022112078001251

Gilliéron, P., & Kourta, A. (2010). Aerodynamic drag reduction by vertical splitter plates. *Experiments in Fluids*, *48*(1), 1–16. https://doi.org/10.1007/s00348-009-0705-7

Gilliéron, P., & Kourta, A. (2013). Aerodynamic drag control by pulsed jets on simplified car geometry. *Experiments in Fluids*, *54*(2), 1457. https://doi.org/10.1007/s00348-013-1457-y

Grandemange, M., Cadot, O., Courbois, A., Herbert, V., Ricot, D., Ruiz, T., & Vigneron, R. (2015). A study of wake effects on the drag of Ahmed's squareback model at the industrial scale. *Journal of Wind Engineering and Industrial Aerodynamics*, *145*, 282–291. https://doi.org/10.1016/j.jweia.2015.03.004

Grandemange, M., Cadot, O., & Gohlke, M. (2012). Reflectional symmetry breaking of the separated flow over three-dimensional bluff bodies. *Physical Review E - Statistical, Nonlinear, and Soft Matter Physics*, *86*(3), 035302. https://doi.org/10.1103/PhysRevE.86.035302

Grandemange, M., Gohlke, M., & Cadot, O. (2013a). Bi-stability in the turbulent wake past parallelepiped bodies with various aspect ratios and wall effects. *Physics of Fluids*, *25*(9), 095103. https://doi.org/10.1063/1.4820372

Grandemange, M., Gohlke, M., & Cadot, O. (2013b). Turbulent wake past a three-dimensional blunt body. Part 1. Global modes and bi-stability. *Journal of Fluid Mechanics*, *722*, 51–84. https://doi.org/10.1017/jfm.2013.83

Grandemange, M., Gohlke, M., & Cadot, O. (2014). Statistical axisymmetry of the turbulent sphere wake. *Experiments in Fluids*, *55*(11), 1838. https://doi.org/10.1007/s00348-014-1838-x

Grandemange, M., Mary, A., Gohlke, M., & Cadot, O. (2013). Effect on drag of the flow orientation at the base separation of a simplified blunt road vehicle. *Experiments in Fluids*, *54*(5), 1529. https://doi.org/10.1007/s00348-013-1529-z

Grotjans, H., & Menter, F. R. (1998). Wall functions for industrial applications. *Computational Fluid Dynamics*, *98*(1), 2.

Guilmineau, E., Deng, G. B., Leroyer, A., Queutey, P., Visonneau, M., & Wackers, J. (2018). Assessment of hybrid RANS-LES formulations for flow simulation around the Ahmed body. *Computers and Fluids*, *176*, 302–319. https://doi.org/10.1016/j.compfluid.2017.01.005

Haffner, Y., Boreé, J., Spohn, A., & Castelain, T. (2020). Mechanics of bluff body drag reduction during transient near-wake reversals. *Journal of Fluid Mechanics*, *894*, A14. https://doi.org/10.1017/jfm.2020.275

He, K., Minelli, G., Wang, J., Dong, T., Gao, G., & Krajnović, S. (2021a). Numerical investigation of the wake bi-stability behind a notchback Ahmed body. *Journal of Fluid Mechanics*, *926*, A36. https://doi.org/10.1017/jfm.2021.748

He, K., Minelli, G., Wang, J., Gao, G., & Krajnović, S. (2021b). Assessment of LES, IDDES and RANS approaches for prediction of wakes behind notchback road vehicles. *Journal of Wind Engineering and Industrial Aerodynamics*, *217*, 104737. https://doi.org/10.1016/j.jweia.2021.10473

He, K., Minelli, G., Su, X., Gao, G., & Krajnović, S. (2021c). Blockage influence on bi-stable flows of a notchback bluff body. *Physics of Fluids*, *33*(12), 125113. https://doi.org/10.1063/5.0077251

He, K., Minelli, G., Su, X., Gao, G., & Krajnović, S. (2021d). Influence of the rounded rear edge on wake bi-stability of a notchback bluff body. *Physics of Fluids*, *33*(11), 115107. https://doi.org/10.1063/5.0071925

He, K., Minelli, G., Su, X., Gao, G., & Krajnović, S. (2022a). On state instability of the bi-stable flow past a notchback bluff body. *Journal of Fluid Mechanics*, *931*, R6. https://doi.org/10.1017/jfm.2021.1025

He, K., Minelli, G., Su, X., Wang, J., Gao, G., & Krajnović, S. (2022b). Floor motion's influence on wake asymmetry of a notchback bluff body. *Physics of Fluids*, *34*(3), 035103. https://doi.org/10.1063/5.0084435

Jahanmiri, M., & Abbaspour, M. (2011). Experimental investigation of drag reduction on Ahmed car model using a combination of active flow control methods. *IJE Transactions A: Basics*, *24*, 403–410. https://doi.org/10.5829/idosi.ije.2011.24.04a.09

Jones, W. P., & Launder, B. E. (1972). The prediction of laminarization with a two-equation model of turbulence. *International Journal of Heat and Mass Transfer*, *15*(2), 301–314. https://doi.org/10.1016/0017-9310(72)90076-2

Joseph, P., Amandolese, X., Edouard, C., & Aider, J. L. (2013). Flow control using MEMS pulsed micro-jets on the Ahmed body. *Experiments in Fluids*, *54*(1), 1442. https://doi.org/10.1007/s00348-012-1442-x

Kang, N., Essel, E. E., Roussinova, V., & Balachandar, R. (2021). Effects of approach flow conditions on the unsteady three-dimensional wake structure of a square-back Ahmed body. *Physical Review Fluids*, *6*(3), 034613. https://doi.org/10.1103/PhysRevFluids.6.034613

Khalighi, B., Chen, K. H., & Iaccarino, G. (2012). Unsteady aerodynamic flow investigation around a simplified square-back road vehicle with drag reduction devices. *Journal of Fluids Engineering, Transactions of the ASME*, *134*(6), 061101. https://doi.org/10.1115/1.4006643

Kim, D., Do, H., & Choi, H. (2020). Drag reduction on a three-dimensional model vehicle using a wire-to-plate DBD plasma actuator. *Experiments in Fluids*, *61*(6), 135. https://doi.org/10.1007/s00348-020-02961-3

Krajnović, S., & Davidson, L. (2004). Exploring the flow around a simplified bus with large eddy simulation and topological tools. In R. McCallen, F. Browand, & J. Ross (Eds.), *The*

Aerodynamics of Heavy Vehicles: Trucks, Buses, and Trains (pp. 49–64). Springer Berlin Heidelberg.

Krajnović, S., & Davidson, L. (2005a). Flow around a simplified car, part 1: Large eddy simulation. *Journal of Fluids Engineering, Transactions of the ASME*, *127*(5), 907–918. https://doi.org/10.1115/1.1989371

Krajnović, S., & Davidson, L. (2005b). Flow around a simplified car, part 2: understanding the flow. *Journal of Fluids Engineering, Transactions of the ASME*, *127*(5), 919–928. https://doi.org/10.1115/1.1989372

Launder, B. E., & Spalding, D. B. (1974). The numerical computation of turbulent flows. *Computer Methods in Applied Mechanics and Engineering*, *3*, 269–289.

Lien, F.-S., Kalitzin, G., & Durbin, P. (1998). RANS modeling for compressible and transitional flows. *Proceedings of the Summer Program 1998*, *Vol 1*, 1998.

Lucas, J. M., Cadot, O., Herbert, V., Parpais, S., & Délery, J. (2017). A numerical investigation of the asymmetric wake mode of a squareback Ahmed body - Effect of a base cavity. *Journal of Fluid Mechanics*, *831*, 675–697. https://doi.org/10.1017/jfm.2017.654

Manceau, R., & Hanjalić, K. (2002). Elliptic blending model: A new near-wall Reynolds-stress turbulence closure. *Physics of Fluids*, *14*(2), 744–754. https://doi.org/10.1063/1.1432693

Pavia, G., Passmore, M., & Sardu, C. (2018). Evolution of the bi-stable wake of a square-back automotive shape. *Experiments in Fluids*, *59*(1), 20. https://doi.org/10.1007/s00348-017-2473-0

Pearson, D. S., Goulart, P. J., & Ganapathisubramani, B. (2013). Turbulent separation upstream of a forward-facing step. *Journal of Fluid Mechanics*, *724*, 284–304. https://doi.org/10.1017/jfm.2013.113

Plumejeau, B., Keirsbulck, L., Delprat, S., Lippert, M., & Abassi, W. (2020). Behavior of the square-back Ahmed body global modes at low ground clearance. *Physical Review Fluids*, *5*(8), 084701. https://doi.org/10.1103/PhysRevFluids.5.084701

Rao, A., Minelli, G., Basara, B., & Krajnović, S. (2018). On the two flow states in the wake of a hatchback Ahmed body. *Journal of Wind Engineering and Industrial Aerodynamics*, *173*, 262–278. https://doi.org/10.1016/j.jweia.2017.10.021

Rodi, W. (1991). Experience with two-layer models combining the k-epsilon model with a one-equation model near the wall. In *29th Aerospace Sciences Meeting*. American Institute of Aeronautics and Astronautics. https://doi.org/doi:10.2514/6.1991-216

Rouméas, M., Gilliéron, P., & Kourta, A. (2009). Drag reduction by flow separation control on a car after body. *International Journal for Numerical Methods in Fluids*, *60*(11), 1222–1240. https://doi.org/10.1002/fld.1930

Shih, T.-H., Liou, W. W., Shabbir, A., Yang, Z., & Zhu, J. (1995). A new k-ϵ eddy viscosity model for high reynolds number turbulent flows. Computers & Fluids, 24(3), 227–238. https://doi.org/https://doi.org/10.1016/0045-7930(94)00032-T

Siddiqui, N. A., & Agelin-Chaab, M. (2022). Experimental investigation of the flow features around an elliptical Ahmed body. *Physics of Fluids*, *34*(10), 105119. https://doi.org/10.1063/5.0114377

Siemens Digital Industries Software. (2021). Simcenter STAR-CCM+ User Guide, version 2021.1. In *Version 10.06.010.* Siemens.

Sims-Williams, D., Marwood, D., & Sprot, A. (2011). Links between notchback geometry, aerodynamic drag, flow asymmetry and unsteady wake structure. *SAE International Journal of Passenger Cars - Mechanical Systems*, *4*(1), 156–165. https://doi.org/10.4271/2011-01-0166

Spalart, P., & Allmaras, S. (1992). A one-equation turbulence model for aerodynamic flows. In *30th Aerospace Sciences Meeting and Exhibit*. American Institute of Aeronautics and Astronautics. https://doi.org/doi:10.2514/6.1992-439

Speziale, C. G., Sarkar, S., & Gatski, T. B. (1991). Modelling the pressure–strain correlation of turbulence: an invariant dynamical systems approach. *Journal of Fluid Mechanics*, *227*, 245–272. https://doi.org/10.1017/S0022112091000101

Strachan, R. K., Knowles, K., & Lawson, N. J. (2007). The vortex structure behind an Ahmed reference model in the presence of a moving ground plane. *Experiments in Fluids*, *42*(5), 659–669. https://doi.org/10.1007/s00348-007-0270-x

Tounsi, N., Mestiri, R., Keirsbulck, L., Oualli, H., Hanchi, S., & Aloui, F. (2016). Experimental study of flow control on bluff body using piezoelectric actuators. *Journal of Applied Fluid Mechanics*, *9*(2), 827–838. https://doi.org/10.18869/acadpub.jafm.68.225.24488

Verzicco, R., Fatica, M., Iaccarino, G., Moin, P., & Khalighi, B. (2002). Large eddy simulation of a road vehicle with drag-reduction devices. *AIAA Journal*, *40*(12), 2447–2455. https://doi.org/10.2514/2.1613

Vino, G., Watkins, S., Mousley, P., Watmuff, J., & Prasad, S. (2005). Flow structures in the near-wake of the Ahmed model. *Journal of Fluids and Structures*, *20*(5), 673–695. https://doi.org/10.1016/j.jfluidstructs.2005.03.006

Volpe, R., Devinant, P., & Kourta, A. (2015). Experimental characterization of the unsteady natural wake of the full-scale square back Ahmed body: flow bi-stability and spectral analysis. *Experiments in Fluids*, *56*(5), 1–22. https://doi.org/10.1007/s00348-015-1972-0

Wilcox, D. C. (1998). *Turbulence Modeling for CFD* (Vol. 2). DCW industries La Canada, CA.

Yu, Z., & Bingfu, Z. (2021). Recent advances in wake dynamics and active drag reduction of simple automotive bodies. In *Applied Mechanics Reviews* (Vol. 73, Issue 6). American Society of Mechanical Engineers (ASME). https://doi.org/10.1115/1.4053132

Zhang, B. F., Liu, K., Zhou, Y., To, S., & Tu, J. Y. (2018). Active drag reduction of a high-drag Ahmed body based on steady blowing. *Journal of Fluid Mechanics*, *856*, 351–396. https://doi.org/10.1017/jfm.2018.703